

1 **Significant influence of oxygenated volatile organic compounds**
2 **on atmospheric chemistry: A case study in a typical industrial city in**
3 **China**

4 Jingwen Dai ^a, Kun Zhang ^{a,*}, Yanli Feng ^a, Xin Yi ^a, Rui Li ^a, Jin Xue ^a, Qing Li ^a, Lishu Shi
5 ^a, Jiaqiang Liao ^a, Yanan Yi ^a, Fangting Wang ^a, Liumei Yang ^a, Hui Chen ^a, Ling Huang ^a,
6 Jiani Tan ^a, Yangjun Wang ^a, Li Li ^{a,*}

7 ^a School of Environmental and Chemical Engineering, Shanghai University, Shanghai, 200444,
8 China

9
10 *Correspondence:* Li Li (Lily@shu.edu.cn) and Kun Zhang (zk1231@shu.edu.cn)

11 **Abstract**

12 Oxygenated volatile organic compounds (OVOCs), an important subgroup of volatile organic
13 compounds (VOCs), are emitted directly or formed secondarily through photochemical processes.
14 They play a crucial role in tropospheric chemistry as ozone (O₃) precursors. However, due to
15 measurement limitations, the influence of OVOCs on O₃ formation has often been underestimated.
16 In this study, 74 VOCs (including 18 OVOCs) were measured at five representative stations (urban,
17 suburban, industrial, upwind, and downwind stations) in Zibo, an industrial city in the North China
18 Plain. The VOCs level in Zibo ($44.6 \pm 20.9 \times 10^{-9}$) is in the upper-middle range ($> 32 \times 10^{-9}$)
19 compared to previous studies conducted in most Chinese cities, with OVOCs contributing for
20 30.0%~37.8%. The average O₃ formation potential in Zibo is $410.4 \pm 197.2 \mu\text{g m}^{-3}$, with OVOCs
21 being the dominant contributor (31.5%~55.9%). An observation-based model (OBM) was used to
22 access the contributions of chemical production (R_{NetProd}) and emissions/transport ($R_{\text{Emis\&Trans}}$) to
23 individual OVOC. Daytime (8:00-18:00 LT) R_{NetProd} is the highest at the urban site ($5.9 \times 10^{-9} \text{ h}^{-1}$),
24 while nighttime $R_{\text{Emis\&Trans}}$ is most negative at the industrial site ($0.76 \times 10^{-9} \text{ h}^{-1}$). Simulations without

25 OVOCs constraint overestimate OVOCs (42.1~126.5%) and key free radicals (e.g., hydroperoxy
26 radicals (HO_2 , 5.3%~20.4% and organic peroxy radicals (RO_2 , 6.6%~35.1%)), leading to a
27 1.8%~11.9% O_3 overestimation. This overestimation causes an underestimation of hydroxyl radicals
28 (OH) (1.8%~20.9%) and atmospheric oxidizing capacity (3.5%~12.5%). These findings emphasize
29 the importance of comprehensive OVOCs measurements to constrain numerical models, especially
30 in regions with dense anthropogenic emissions, to better reproduce atmospheric photochemistry,
31 and to formulate more effective air pollution control strategies.

32 **1. Introduction**

33 Oxygenated volatile organic compounds (OVOCs), contributing 20.1%~73.5% of total volatile
34 organic compounds (VOCs) (Han et al., 2019; Huang et al., 2020; Li et al., 2022a; Liu et al., 2024;
35 Song et al., 2024), are critical components of tropospheric photochemistry (Yang et al., 2014).
36 Photolysis of OVOCs has been proved to be the most significant primary source of RO_x ($\text{OH} + \text{HO}_2$
37 + RO_2) in Guangzhou, Beijing, and Xi'an in China (Wang et al., 2022c; Yang et al., 2018; Zhang et
38 al., 2021b), and thereby accelerating the recycling of radicals to promote ozone (O_3) formation (Qu
39 et al., 2021; Wang et al., 2022c). In addition, previous studies have shown that sufficient free radicals
40 produced by photolysis of OVOCs are the dominated contributors to O_3 pollution during winter
41 (Edwards et al., 2014; Emmerson et al., 2005). The study of Li et al. (2021b) indicates that the fast
42 generation of O_3 during winter haze in the North China Plain is mainly driven by the photolysis of
43 formaldehyde (HCHO), which leads to a large production of HO_x radical and offsets the radical
44 titration induced by NO_x emissions. In addition, HCHO and other OVOCs dominated the OH loss
45 with VOCs (Goldan et al., 2004), resulting in predominant role in OH reactivity (Ling et al., 2014;
46 Yang et al., 2018). Therefore, OVOCs play a significant role in the atmospheric chemistry.

47 OVOCs have complex and diverse sources, including primary emissions from anthropogenic,
48 e.g., vehicle exhausts (Gentner et al., 2013; Legreid et al., 2007; Wang et al., 2022b), volatile
49 chemical product use (Ou et al., 2015), industries (Wang et al., 2023), biomass combustion (Gilman
50 et al., 2015; Karl et al., 2007; Li et al., 2014a; Yokelson et al., 2007), and biogenic sources (Ou et
51 al., 2015; Rieksta et al., 2023). They are also formed secondarily through photochemical reactions
52 (Huang et al., 2020; Song et al., 2024; Xia et al., 2021). Mo et al. (2016) estimated that OVOCs
53 from heavy-duty diesel vehicle emissions accounted for 53.8% of total VOCs in China, and OVOCs
54 account for 12.4%~46.3% of VOCs emission from biomass and residential coal combustion, which
55 demonstrates the importance of combustion-related sources of OVOCs. In addition, measurement
56 of VOCs fluxes based on the airborne eddy covariance technique showed that urban emission
57 sources comprise a surprisingly large proportion of OVOCs (29%~56%) (Karl et al., 2018;
58 Pfannerstill et al., 2023). Due to the high share of OVOCs in VOCs, previous studies have reported
59 that OVOCs could contributed 38%~60% of ozone formation potential (OFP) (Liu et al., 2024; Mo
60 et al., 2022; Wang et al., 2022a, 2024). The loss of OVOCs occurs through photolysis, reactions
61 with oxidants (e.g., OH, NO₃, and O₃), dilution mixing and deposition (Atkinson, 2000; Atkinson
62 and Arey, 2003). Moreover, air mass transport also can significantly affect the mixing ratio of
63 OVOCs.

64 Chemical transport models (CTMs) have been widely used for the study of formation
65 mechanism of OVOCs and their influence on air quality (Chen et al., 2022; de Gouw et al., 2018;
66 Luecken et al., 2012; Steiner et al., 2008; Yang et al., 2023). However, due to the deviation of the
67 meteorological field, uncertainty of the emission inventory (Li et al., 2019; McDonald et al., 2018;
68 Shen et al., 2019), defects of lumped chemical mechanism (Li et al., 2014b; Sarwar et al., 2008;

69 Stockwell et al., 1997a; Venecek et al., 2018), there is a large uncertainty in the OVOCs simulated
70 by CTMs, which in turn leads to large deviations in the simulated atmospheric photochemistry. The
71 observation-based model (OBM) can avoid these biases to a certain extent by constraining
72 meteorological parameters and chemical species, and leveraging detailed chemical mechanism (e.g.,
73 Master chemical mechanism, MCM). Nevertheless, due to the limited observations of OVOCs (e.g.,
74 Pfannerstill et al., 2023), many existing studies use OBM without the observed OVOCs data, or
75 only with limited inputs for certain OVOCs species (formaldehyde, acetaldehyde, acetone), which
76 can greatly bias the assessment of O₃ generation mechanism, free radical chemistry, and atmospheric
77 oxidation. Wang et al. (2022a) showed that the box model without the constraint of OVOCs
78 underestimates the OVOCs concentrations, which in turn lead to the underestimation of RO_x and O₃
79 formation. Thus, it is meaningful to couple OVOCs observation with OBM to investigate how
80 OVOCs affect radical chemistry, atmospheric oxidization capability, and O₃ formation mechanism.

81 Zibo, a typical industrial cluster city in China, has been suffering from O₃ pollution for years
82 (Li et al., 2021a; Qin et al., 2023). However, comprehensive studies involving the observation of
83 VOCs, particularly OVOCs such as HCHO, are rare. Qin et al. (2023) used observations of 98 VOCs
84 (without HCHO) in Zibo to constrain OBM, but the absence of HCHO in their simulation could
85 result in underestimation RO_x, thus disturbing the investigation of OH budget (Fuchs et al., 2017;
86 Guo et al., 2021; Ling et al., 2014; Qu et al., 2021; Tan et al., 2017). This study hypothesizes that
87 incorporating observational constraints on OVOCs significantly influences the OBM simulations.
88 To evaluate this, a 5-day field campaign was conducted across five representative sites in Zibo.
89 Concentrations of 74 VOC species, including 29 alkanes, 16 aromatics, 9 alkenes, 18 OVOCs,
90 acetylene and isoprene, are obtained. The contributions of secondary formation, emissions/transport

91 to OVOCs level are analyzed by the OBM. Additionally, the impact of OVOCs on radical chemistry,
92 atmospheric oxidation capability, and consequently O₃ production are quantified.

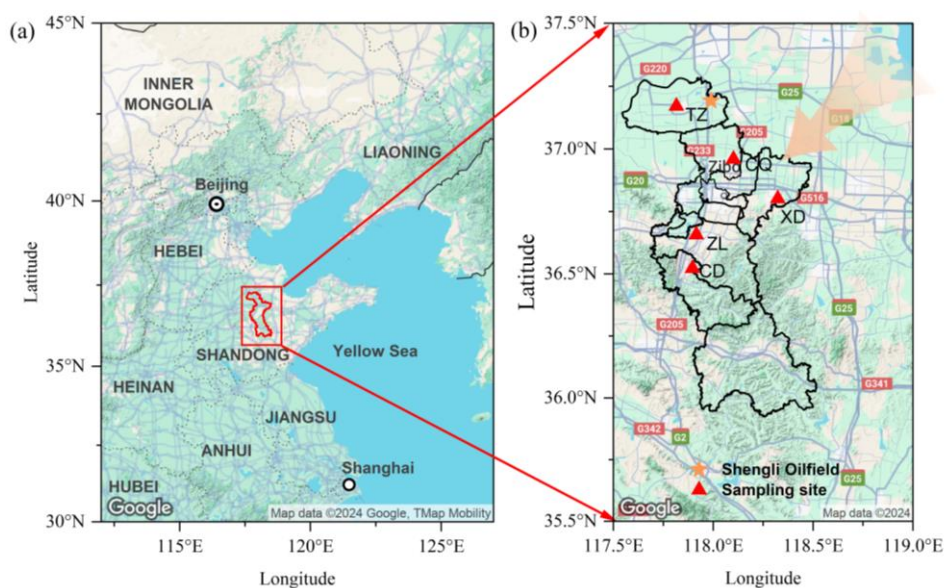
93 **2. Methodology**

94 **2.1 Sampling sites and measurements**

95 To capture a typical ozone pollution case, the field campaign was conducted from August 8 to
96 August 12, 2021, at five monitoring sites (Zhonglou (ZL), Chengdong (CD), Chengqu (CQ),
97 Tianzhen (TZ), and Xindian (XD)) in Zibo (Figure 1, Table S1). Among the five sites, ZL site
98 (117°54'E, 36°39'N) is an urban site, which is located in the central area of Zibo, and is mainly
99 surrounded by residential areas and factory buildings. According to the prevailing wind direction
100 (northeast, Figure S1 (a)), CQ (118°60'E, 36°57'N) site is an upwind site, while CD (117°53'E,
101 36°31'N) is a downwind site. CD is located on a hillside in the southern part of Zibo, with a small
102 number of ceramic and refractory enterprises factories nearby. TZ (117°48'E, 37°10'N) is close to
103 Shengli Oil field on the west, and is surrounded by farmland. This site is regarded as a suburban site
104 and is affected by residential emissions in the north of Zibo, as well as nearby oil production
105 operations. XD (118°19'E, 36°48'N) is close to a chemical industrial park and serves as an industrial
106 site. More detailed information about these sites can be found in Table S1.

107 Site-scale wind patterns can affect the levels and spatial distribution of OVOCs and PAMS
108 (target VOC species from the Photochemical Assessment Monitoring Stations, including include 29
109 alkanes, 16 aromatics, 9 alkenes, isoprene, and acetylene) across sites. Urban (ZL) and downwind
110 (CD) sites are impacted by OVOC pollution from northeasterly (NNE, NE, ENE) winds, while the
111 upwind (CQ) site experiences higher OVOC and VOCs pollution under both northeasterly and
112 northwesterly (WNW, NW, NNW) winds (Figure S2 (a, b)). Suburban (TZ) and industrial (XD)

113 sites exhibited higher OVOC and VOCs levels under southeasterly (SE) and southwesterly (WSW)
114 winds, respectively, likely due to upwind emissions from nearby industrial sources. WS between 1
115 and 2 m s^{-1} were most common (40.4%) during the observation period. At suburban (TZ) and
116 industrial (XD) sites, OVOC and VOCs levels were lower at low wind speeds ($WS < 2 \text{ m s}^{-1}$) than
117 that at higher wind speeds, reflecting the influence of local emissions (Figure S2(c, d)). In contrast,
118 at downwind (CD) site, higher OVOC and VOCs levels were observed at $WS > 2 \text{ m s}^{-1}$, indicating
119 the impact of regional transport. At the urban (ZL) site, higher WS are associated with lower VOCs
120 levels and higher OVOC levels, indicating the influence of aging air masses transported from
121 upwind regions.



122
123 **Figure 1. (a) Map of the North China Plain and (b) map of Zibo with locations of VOCs monitoring stations**
124 **(red triangles), and Shengli Oil field (yellow star), and prevailing wind direction (orange arrow).**

125 During the campaign, two online gas chromatography-flame ionization detector (GC-FID,
126 Thermo Scientific GC5900) systems were deployed at suburban (TZ) and upwind (CQ) stations,
127 and three online gas chromatography-flame ionization detector (GC-FID, Syntech Spectras GC
128 955–615/815) systems were deployed at downwind (CD), industrial (XD) and urban (ZL) stations,
129 respectively. A mixture of 56 PAMS target species (Spectra Gases Inc., USA, Table S2) was used

130 for the calibration of the GC-FID system. Each VOC analyzer provided measurements with a 1-
131 hour temporal resolution. More detailed descriptions of these instruments can be found in previous
132 studies (Li et al., 2023; Wang et al., 2014; Yang et al., 2022; Zheng et al., 2023). Overall, the
133 detection limits for most VOC species are below 0.1×10^{-9} . Additionally, 18 oxygenated VOCs
134 species were collected by 2,4-dinitrophenylhydrazine (DNPH) sorbent tubes in conjunction with an
135 automated sampler for a period of 1 or 3 hour per sample. A 47 mm quartz filter membrane is
136 attached to the front of the sampling tube to filter particulate matter. An ozone scrubber (silica gel
137 column tubing coated with potassium iodide) was placed at the front of the air inlet to avoid ozone
138 interference. OVOCs were derivatized in cartridges to hydrazones during sampling. The cartridges
139 were eluted with 3 mL of acetonitrile and stored at 0-4 °C immediately. Then the eluants were
140 analyzed using an Agilent HPLC, equipped with ultraviolet absorption detector (UVD), quadruple
141 pump, and Agilent TM C18 reversed column (250 mm×4.6 mm, 5.0 μm). A gradient elution was
142 used, and the mobile phase was mixing of acetonitrile, tetrahydrofuran and water. The analysis was
143 carried out using a ternary gradient elution program at a flow rate of 1.2 mL/min, with detection
144 wavelength of 360 nm, and sample volume of 10 μL at a column temperature of 45 °C. More details
145 about OVOC samplings and analysis can be found in Peng et al. (2023). The lower limit of detection
146 for OVOCs were $<0.1 \times 10^{-9}$ (Peng et al., 2023). A total of 271 valid OVOCs samples were collected
147 during the campaign. At the industrial (XD) and suburban (TZ) stations, 8 samples were collected
148 per day at 3-hour intervals. At the urban (ZL), upwind (CQ) and downwind (CD) stations, 10
149 samples were collected per day, with 7 samples collected at 1-hour intervals during 7:00-21:00 LT,
150 and 3 samples collected at 3-hour intervals during the night (1:00-6:00 and 22:00-1:00⁺¹ LT), and
151 totaling 59 valid samples per station. Finally, a total of 74 VOCs (56 PAMS and 18 OVOCs) were

152 combined to conduct data analysis in this study (Table S2). Conventional gas phase pollutants (e.g.,
153 O₃, CO, and NO_x (NO and NO₂)) were measured using commercial online analyzers (Thermo
154 Scientific 49i, 48i, and 42i, USA) at each site. NO_x was measured by NO chemiluminescence and
155 chemical conversion with a molybdenum convertor, which is known to be interfered by NO_z species
156 (Tan et al., 2017, 2019a). Meteorological parameters, including temperature (T), relative humidity
157 (RH), wind speed (WS), wind direction (WD), and ambient pressure (P) were obtained
158 synchronously by Chinese ground-based meteorological stations (Boshan, Huantai, Gaoqing, Linzi,
159 and Zichuan sites) (<http://data.cma.cn/>, last access: March 26, 2024).

160 **2.2 Observation-based model**

161 A box model (F0AM) coupled with the Master Chemical Mechanism (MCM) v3.3.1 was
162 utilized to simulate the in situ atmospheric chemical process at these 5 sites (Jenkin et al., 2015;
163 Wolfe et al., 2016). The MCMv3.3.1, as a nearly explicit mechanism with more than 5800 species
164 and 17000 reactions, provides a more detailed gas chemistry than other lumped mechanisms, such
165 as the Carbon Bond Mechanism (CB) (Yarwood et al., 2005, 2010), Regional Atmospheric
166 Chemistry Mechanism (RACM) (Goliff et al., 2013; Stockwell et al., 1997b), and SAPRC (Carter,
167 1990, 2010b; Carter and Heo, 2013). The box model calculations were constrained by
168 comprehensive measurements of trace gases (NO, NO₂, CO, and SO₂) and 45 speciated VOCs,
169 encompassing 20 alkanes, 9 alkenes, 14 aromatics, 15 OVOCs, isoprene and acetylene, as well as
170 meteorological parameters (T, RH and P). To address potential NO₂ measurement artifacts, several
171 adjustments were implemented. Considering that PKU-Mo as a catalytic converter for NO₂
172 measurement can cause interferences from other nitrogen–oxygen compounds (e.g., PAN, HNO₃),
173 potentially overestimating NO₂ by 30%~50% (Kim et al., 2015; Tan et al., 2017, 2019a; Xu et al.,

174 2013). In this study, the observed NO₂ concentrations at the 5 sites were reduced by 30%~40% (40%
175 for ZL and CQ, 30% for CD, TZ and XD) to compensate for catalytic converter interferences (Xu
176 et al., 2013). Additionally, strong anthropogenic emissions (e.g., vehicle emissions) near the sites
177 may prevent the model from reaching steady state, leading to positive deviations (Li et al., 2014c).
178 Therefore, NO steady-state approximations (NO_{ss}), calculated according to the equations proposed
179 by Del Negro et al. (1999) (Equation S1), was used to constrain the simulated NO. The uncertainties
180 derived from the NO_x settings are shown in Table S3 and analyzed in Section 3.4. HONO was fixed
181 to 2% of the corrected NO₂ mixing ratio (Elshorbany et al., 2012; Tan et al., 2019a), and the
182 corresponding uncertainty is summarized in Section 3.4. In addition, boundary layer height (BLH),
183 and surface net solar radiation (SSR) were obtained from the fifth generation of the European Centre
184 for Medium-Range Weather Forecasts (ECMWF) reanalysis for the global climate and weather
185 (<https://cds.climate.copernicus.eu>, last access: March 1, 2024). The photolysis frequency correction
186 factor (Jcorr) of the model input was adjusted by SSR. BLH was also included in the model to
187 control the deposition process (Xuan et al., 2023; Zhu et al., 2020).

188 The model ran with continuous time series profile for the campaign period (August 8-12) with
189 1-hour time-step. A sensitivity analysis was performed for the time-step and the results are
190 summarized in Section 3.4. Each simulation started with 10-days spin up to reach steady state
191 condition. Missing observation data were filled with linear interpolation, and the mixing ratios of
192 OVOCs were also linearly interpolated to 1-hour resolution for modeling. An artificial loss process
193 corresponding to an atmospheric lifetime of 24 h or a first-order dilution rate (kdil) of 1/86400 s⁻¹
194 was introduced for all simulated species, including secondary species and radicals, to approximately
195 simulate dry deposition and other losses (Lou et al., 2010; Tan et al., 2018b; Wang et al., 2022c).

196 The model cases that run with the above settings with 15 constrained OVOCs species are called the
197 Base scenario. To investigate the impacts of constrains of OVOCs on atmospheric chemistry, the
198 Free scenario was conducted, with all the setting of the Base scenario except for the OVOCs
199 constraint.

200 **2.3 Budgets of OVOCs and O₃**

201 At a given site, variations in OVOCs mixing ratios are mainly influenced by in-situ
202 photochemical production and chemical loss, emissions, regional transport, and deposition (Tan et
203 al., 2018a; Xue et al., 2014a; Zhang et al., 2021). The change rate of observed OVOCs (R_{Meas}) is
204 calculated by Equation (1). The in-situ photochemical production of OVOC ($R_{ChemProd}$) is mainly
205 caused by the oxidation of VOCs, while their in-situ chemical loss ($R_{ChemLoss}$) includes photolysis
206 and reactions with oxidants (OH, NO₃, and O₃) (<https://mcm.york.ac.uk/MCM/>, last access: 13 Jan
207 2025) (Atkinson, 2000; Atkinson and Arey, 2003; Jenkin et al., 2015; Saunders et al., 2003). The in-
208 situ net OVOCs chemical production ($R_{NetProd}$) (Equation (2)) and their removal by deposition (R_{Deps})
209 are calculated hourly according to the OBM simulation. The OBM primarily accounts for
210 atmospheric photochemical reactions, and deposition within the boundary layer. However, previous
211 studies have reported that the OBM lacks an explicit representation of transport processes and
212 emissions (Wolfe et al., 2016; Zhang et al., 2021), making it challenging to disentangle their
213 respective contributions. Therefore, emissions and transport are combined to a single term
214 ($R_{Emis\&Trans}$) to represent their contributions collectively. If the $R_{Emis\&Trans}$ is positive, it is considered
215 a net import of emissions/transport, whereas a negative suggests a net export. The emissions and
216 regional transport of OVOCs ($R_{Emis\&Trans}$) are computed as Equation (3).

$$R_{Meas} = \sum_i \frac{d([OVOC]_i)}{dt} \quad (1)$$

$$R_{NetProd} = \sum_i (R_{ChemProd,i} - R_{ChemLoss,i}) \quad (2)$$

$$R_{Emis&Trans} = (R_{Meas} - R_{NetProd} - \sum_i R_{Deps,i}) \quad (3)$$

217 where $[OVOC]_i$ is the mixing ratios of OVOC species i constrained in OBM, 15 in total (Table S2).

218 dt is the time-step of modeling, $d[OVOC]_i$ refer to the change in mixing ratio of OVOC species i .

219 Considering the oxidation of NO to NO₂ by peroxy radicals, the total oxidant ($O_x = O_3 + NO_2$)

220 is generally used to characterize the chemical budget of O₃ (Kanaya et al., 2009; Xue et al., 2014b).

221 The total chemical production of O_x through oxidations of NO by HO₂ and RO₂ radicals (Tan et al.,

222 2018b), is defined as the production of O₃ ($P(O_3)$), which is calculated according to Equation (4):

$$P(O_3) = k_{HO_2+NO}[HO_2][NO] + \sum k_{RO_2,j+NO}[RO_2]_j[NO] \quad (4)$$

223 The chemical loss rate ($L(O_3)$) of O₃ is equal to the sum of loss rates of O₃ and NO₂, including

224 O₃ photolysis, reactions of O₃ with OH, HO₂ and alkenes, as well as reactions of NO₂ with OH and

225 RO₂, as well as the reaction of NO₃ with unsaturated VOCs (Chen et al., 2020; Liu et al., 2022; Xue

226 et al., 2016, 2014b).

$$\begin{aligned} L(O_3) = & k_{O_1D+H_2O}[O_1D][H_2O] + k_{O_3+OH}[O_3][OH] \\ & + k_{O_3+HO_2}[O_3][HO_2] + k_{O_3+alkenes}[O_3][alkenes] \\ & + k_{NO_2+OH}[NO_2][OH] \\ & + \sum k_{NO_2+RO_2,j}[NO_2][RO_2]_j \\ & + \sum k_{NO_3+VOC,i}[NO_3][VOC]_i \end{aligned} \quad (5)$$

227 The concentrations of radicals and intermediates are derived from the outputs of the OBM. The

228 k values in Equations (4) and (5) rate constants of the corresponding reactions, which can be found

229 from <https://mcm.york.ac.uk/MCM/> (last access: 13 Jan 2025) or the study by Liu et al. (2022). The

230 subscript ' j ' in Equation (4) and (5) denotes individual RO₂ species. The subscript ' i ' in Equation

231 (5) represents individual VOC species. The net O₃ production rate can be obtained from the
232 difference between P (O₃) and L(O₃).

233 **2.4 Evaluation of ozone formation potential and atmospheric oxidation capacity**

234 Different VOC species vary in their capability to form ozone, and their potential to produce O₃
235 can be evaluated by the maximum incremental reactivity (MIR) (Carter, 2010a). The ozone
236 formation potential (OFP) calculated for each VOC species represents its maximum contribution to
237 ozone production (Bufalini and Dodge, 1983). The OFP of VOCs is calculated as follows:

$$OFP_i = [VOC]_i \times MIR_i \quad (6)$$

238 where OFP_i is the OFP of VOC species i ($\mu\text{g m}^{-3}$), $[VOC]_i$ is the atmospheric concentration of VOC
239 species i ($\mu\text{g m}^{-3}$), MIR_i is the maximum incremental reactivity coefficient of the VOC species i (g
240 O₃/g VOCs) (Table S2) from Carter, 2010a.

241 Atmospheric oxidation capacity (AOC) is the core driving force of complex air pollution,
242 influencing the removal rate of trace gases and the production rates of secondary pollutants (Liu et
243 al., 2021). AOC is calculated based on the sum of oxidation rates of oxidants (OH, O₃, and NO₃)
244 with primary pollutants (VOCs, CO, and CH₄) (Elshorbany et al., 2009; Geyer et al., 2001; Yang et
245 al., 2022b). The formula is as follows:

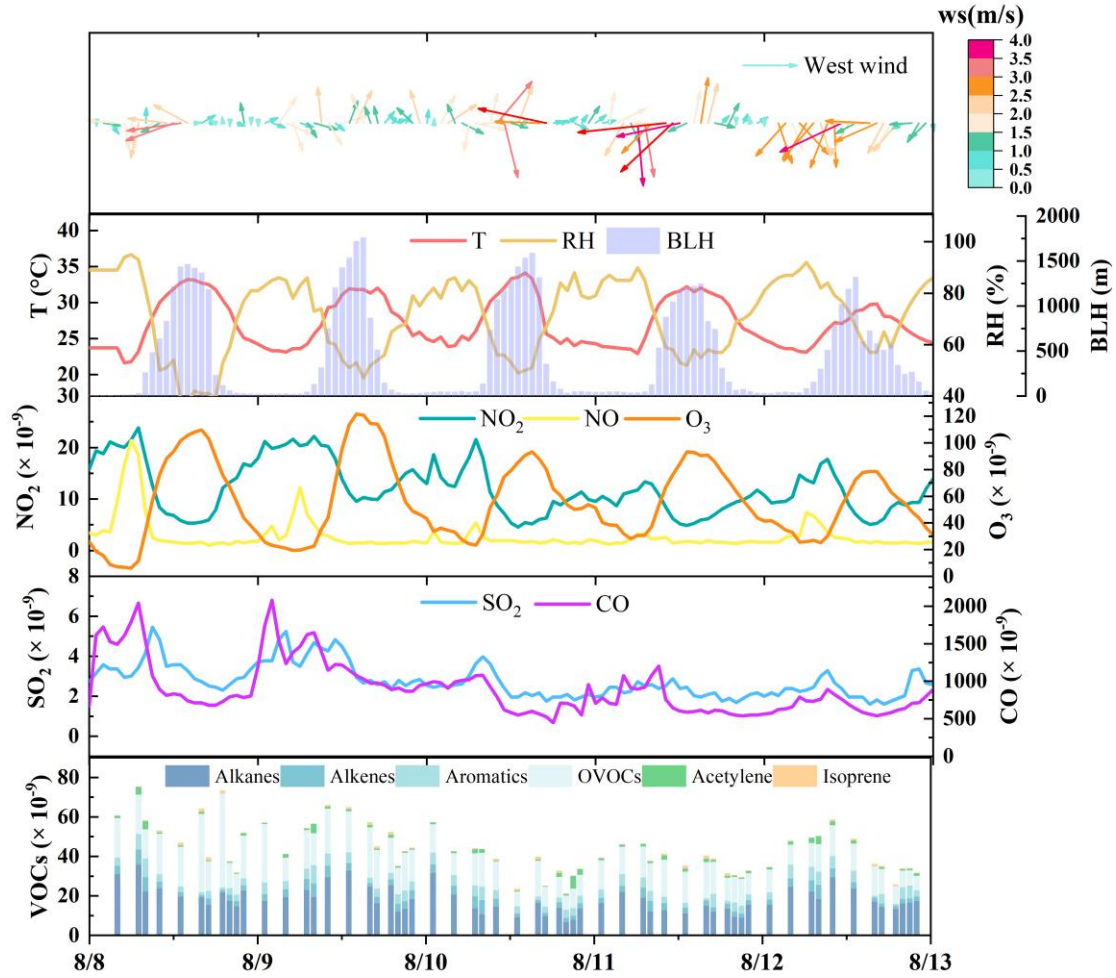
$$AOC = \sum_i k_{Y_i} [Y_i] [X] \quad (7)$$

246 where Y_i represents primary VOCs (excluding OVOCs), CO and CH₄, X represents oxidants (OH,
247 O₃ and NO₃) and k_{Y_i} is the bimolecular rate constant for the reaction of Y_i with X . Atmospheric
248 oxidation capacity determines the rate of Y_i removal.

249 **3. Results and discussion**

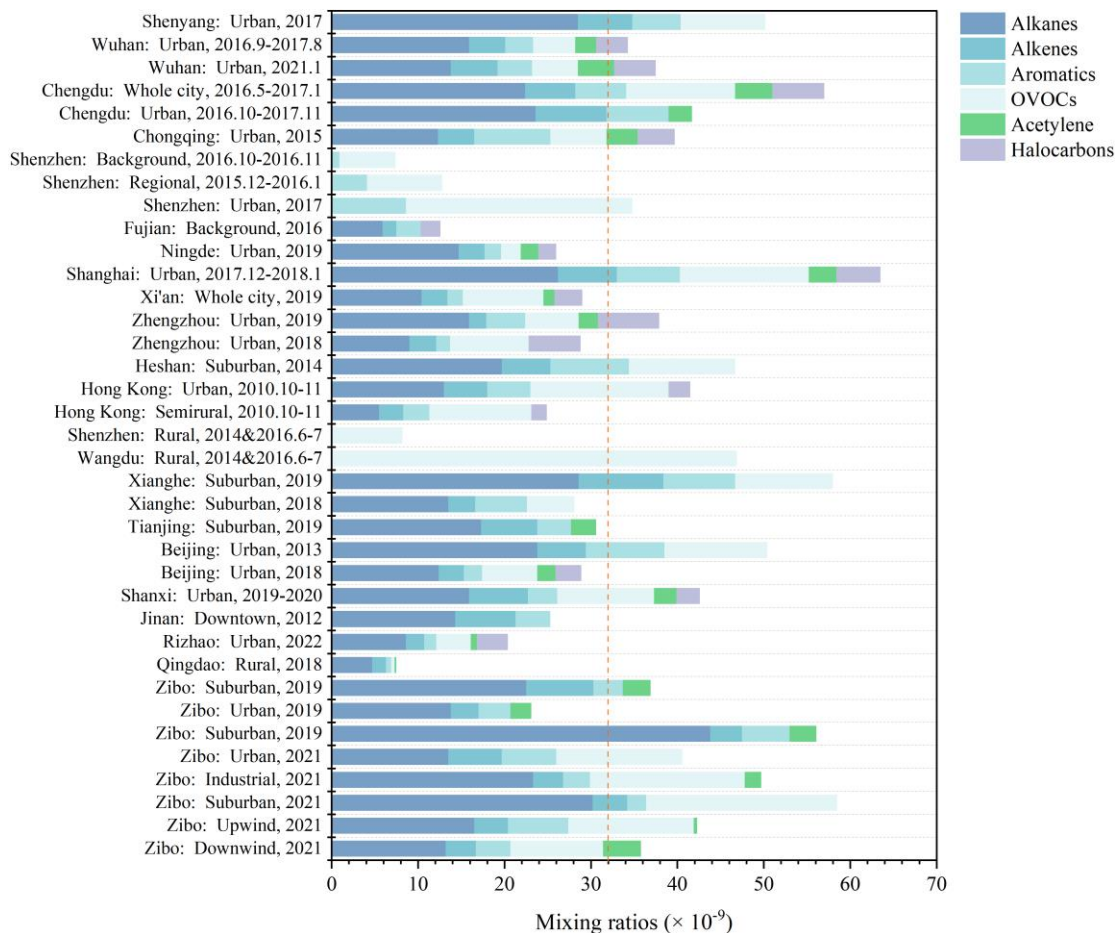
250 **3.1 Meteorological and chemical conditions**

251 The field campaign is characterized by consistent hot and sunny conditions, with the average
252 daily maximum temperature and SSR of 32.2 ± 1.4 °C (peak at 34.1 °C) and $2.1 \pm 0.4 \times 10^6$ J m⁻²
253 (Figure 2, Figure S2 (a)), respectively, which favors the photochemical formation of O₃. A typical
254 O₃ episode was observed, with an average maximum daily 8-hour average O₃ (MDA8-O₃) of 89.8
255 $\times 10^{-9}$ in Zibo city. According to the Chinese National Ambient Air Quality Standard Grade II (about
256 93.3×10^{-9} for 1-hour average, or 74.7×10^{-9} for MDA8-O₃), there are four O₃ pollution days
257 (August 8 to 11) during the campaign. The average mixing ratios of SO₂, NO₂, NO, and CO in Zibo
258 are 2.8 ± 1.6 , 12.0 ± 6.9 , 2.8 ± 4.8 , and $897 \pm 670 \times 10^{-9}$, respectively (Figure 2, Figure S3 (b)). The mean
259 VOCs mixing ratio in this study is $44.6 \pm 20.9 \times 10^{-9}$, which is overall higher than that in Beijing
260 ($18.3 \pm 8.9 \times 10^{-9}$) from July 23 to August 31 in 2016 (Wu et al., 2023), Rizhao (9.83×10^{-9}) in
261 summer in 2022 (Zhang et al., 2023), and Xi'an ($29.1 \pm 8.4 \times 10^{-9}$) from June 20 to July 2019 (Song
262 et al., 2021). Compared with the median VOC levels ($\sim 32 \times 10^{-9}$) in other cities in China (Figure 3,
263 Table S4), VOC levels in Zibo is in the upper-middle range. Previous studies have demonstrated
264 that industrial processes account for approximately 49% of total VOC emissions in Shandong
265 Province (Jiang et al., 2020; Li et al., 2017; Ren, 2011; Zheng et al., 2021). This indicates strong
266 anthropogenic VOCs emission in Zibo. Notably, VOC emission intensity in Zibo was among the
267 highest in Shandong Province, with values > 90 t km⁻² y⁻¹, even > 108 t km⁻² y⁻¹ in some areas in
268 2016 (Jiang et al., 2020; Zhou et al., 2021). In terms of the VOCs groups (Figure 5 (c), Figure S4
269 (a)), alkanes and OVOCs were the two predominant groups at each site, accounting for 33.3~51.5%
270 and 30.0~37.8% to the total VOCs, respectively, followed by aromatics (3.8~16.5%) and alkenes
271 (5.0~13.8%). In addition, the difference between peak and valley NO₂ mixing ratios was 14.4 ± 3.2
272 $\times 10^{-9}$, indicating that substantial NO_x was converted to O₃.



273
 274
 275
 276
 277
 278

Figure 2. Time profiles of pollutant mixing ratios and meteorological parameters in Zibo from August 8 to 12, 2021. The meteorological data were from ZL, the central site of Zibo, and the pollutants data were the average of the five sites. The hourly PAMS (including alkanes, alkenes, aromatics, acetylene, and isoprene) data were aligned with the 1/3-hour sampling intervals of the OVOCs data to ensure comparability between the two datasets.

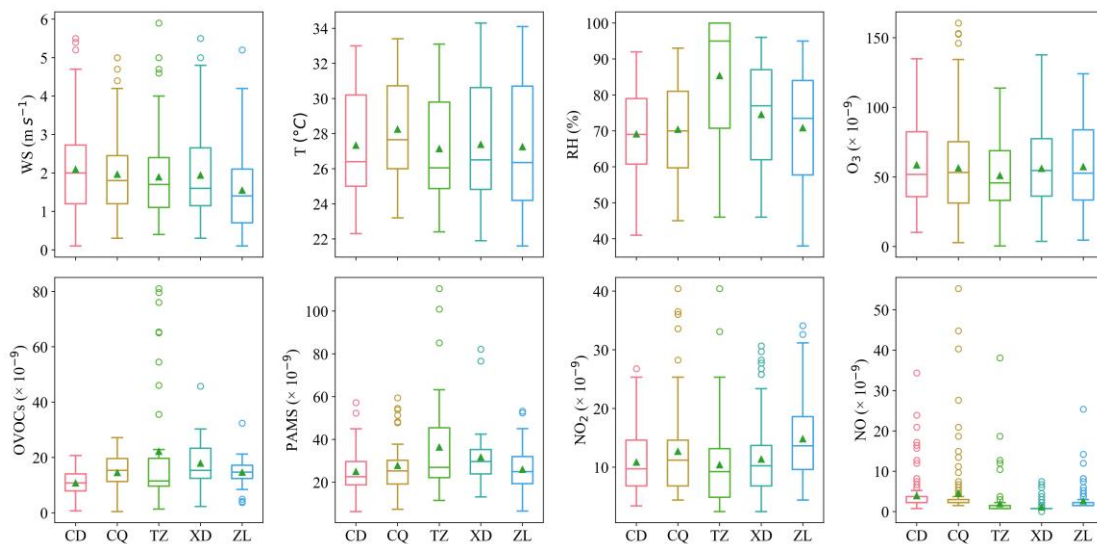


279

280

281

Figure 3. Comparison of VOCs mixing ratios and compositions in this study with former studies based on Table S4. The red dash line represents the median levels ($\sim 32 \times 10^{-9}$) of VOCs.



282

283

284

285

Figure 4. Distribution of O_3 and its precursors (OVOCs, PAMS, NO_2 , and NO) and meteorological parameters (WS, T, and RH) at five sites, with the green triangle being the mean value and the horizontal line in the box being the median.

286

Across the five sites, the O_3 mixing ratios are comparable across all the sites (Table S6, Table

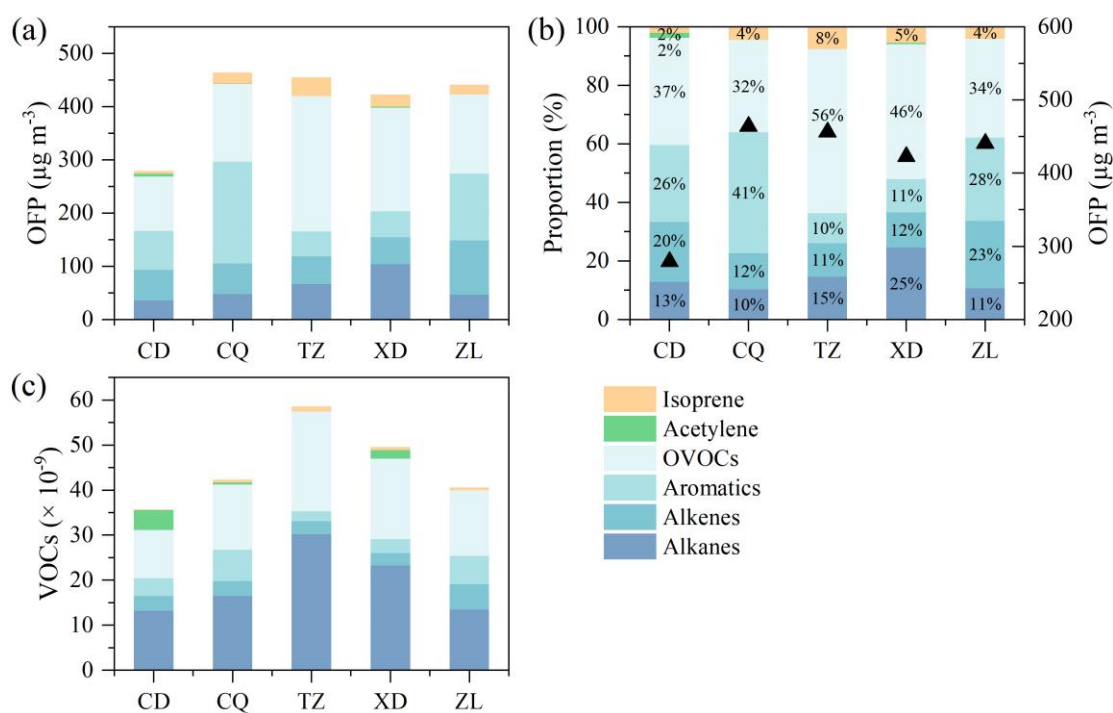
287 S11) ($p > 0.05$). However, TVOCs at suburban site (TZ, $58.5 \pm 35.0 \times 10^{-9}$) is the highest (Figure 5
288 (c), Figure S4 (b)), which is attributed to oil refineries near this site. The downwind site (CD) has
289 slightly lower NO_2 level ($10.8 \pm 5.1 \times 10^{-9}$) and lower TVOCs mixing ratios ($35.7 \pm 12.5 \times 10^{-9}$) than
290 urban site (ZL, 14.8 ± 6.5 and $40.6 \pm 10.3 \times 10^{-9}$, respectively) and upwind site (CQ, 12.7 ± 8.1 and
291 $42.3 \pm 15.4 \times 10^{-9}$, respectively), and has higher O_3 mixing ratio ($58.6 \pm 30.0 \times 10^{-9}$) than CQ and ZL
292 station. This may be attributed to the sequential transport of O_3 and its precursors from the upwind
293 station (CQ) to urban station (ZL), and subsequently to the downwind station (CQ), driven by the
294 dominant northeasterly winds (Figure 1 (b), Figure S1).

295 According to the time series of individual pollutant (Figure S3 (b)), CQ showed obvious peak
296 mixing ratios of O_3 , NO_2 , NO and CO than the other sites during August 8-9, with stagnant
297 conditions ($\text{WS} < 2 \text{ m s}^{-1}$), indicating stronger emissions from combustion sources and possibly fast
298 photochemical process near CQ. In addition, XD showed high mixing ratios of CO during August
299 8-9, and high daytime TVOCs levels on August 9 (9:00-14:00 LT, $90 \sim 110 \times 10^{-9}$). Given CO 's
300 relatively inert nature and the absence of similar CO peaks at the other four sites, the abnormal CO
301 peak at XD is related to strong emissions from nearby factories in the industrial park. TZ showed
302 distinct morning and evening peaks of TVOCs at 6:00 LT (163.0×10^{-9}) and 21:00 LT (120.0×10^{-9})
303 on August 8, and a night peak at 1:00 LT on August 10 (130.3×10^{-9}), which were attributed to
304 emissions from the neighboring oil field operations. From August 10 to 12, as wind speeds increased,
305 pollutants levels at all sites decreased to similar levels. Overall, local anthropogenic emissions in
306 Zibo were more prominent under weak wind conditions.

307 To compare the secondary O_3 formation in each site, the ozone formation potential (OFP) of
308 each VOCs is calculated (Equation (6)). The mean OFP in Zibo during the observation is

309 410.4±197.2 $\mu\text{g m}^{-3}$, with OVOCs accounting for the largest proportion (31.5%~55.9%), followed
310 by aromatics (10.2%~41.2%). Alkanes (10.3%~24.6%) and alkenes (11.4%~23.1%) make
311 comparable proportions, while BVOCs accounted for only 2.1%~7.6% of the total OFP (Figure 5
312 (b)). The one-way analysis of variance (ANOVA) results ($p < 0.05$) indicate significant differences
313 (Armstrong et al., 2000) in VOC subclass contribution to OFP across the 5 sites. Alkanes and
314 aromatics show larger F-values (Table S11), reflecting greater variations in the contributions to OFP
315 across the 5 sites, whereas OVOC and BVOC (isoprene) exhibited lower variability. Post-hoc Tukey
316 honestly significant difference (HSD) tests were performed followed ANOVA to further identify
317 specific significant differences in VOC subcategories between sites (Figure S14). The OFP of
318 TVOCs is generally similar across stations, except for the downwind station (CD). The upwind
319 station (CQ, 464.2±162.3 $\mu\text{g m}^{-3}$) has the highest OFP, followed by the suburban site (TZ,
320 456.3±295.3 $\mu\text{g m}^{-3}$), the urban site (ZL, 441.1±174.5 $\mu\text{g m}^{-3}$), the industrial site (XD, 422.9±166.9
321 $\mu\text{g m}^{-3}$), and the downwind site (CD, 279.4±101.2 $\mu\text{g m}^{-3}$) (Table S5). Differences in OFP levels of
322 aromatics and alkanes at downwind station (CD), suburban station (TZ) and industrial station (XD)
323 are minimal (Figure S14 (b, c)). However, significant differences in OFP contributed by OVOC at
324 downwind station (CD) compared to suburban station (TZ) and industrial station (XD) are attributed
325 to OVOC emission sources, regional transport and secondary formation (Figure S14 (a)). Apart from
326 CQ, OVOCs are the dominant contributors to OFP at each site, especially TZ and XD, with mean
327 OFP of 254.9±276.1 $\mu\text{g m}^{-3}$ (55.9%) and 194.7±101.0 $\mu\text{g m}^{-3}$ (46.0%) from OVOCs, respectively.
328 This indicates the key role of OVOCs in the formation of O_3 at our observational sites. Among
329 OVOC species, HCHO is the dominant contributor to OFP across the five sites (56.6~202.0 $\mu\text{g m}^{-3}$).
330 This is consistent with previous studies (Duan et al., 2008; Huang et al., 2020; Zhou et al., 2024).

331 The top four OVOC species are formaldehyde, acetaldehyde, propionaldehyde, and butyraldehyde,
 332 which cumulatively contributed 91%–95% of the OFP from OVOCs (Table S5). Additionally, the
 333 variety of VOCs sources, meteorological condition, and photochemical condition in each site lead
 334 to differences in key species of OFP at each site. At the suburban site (TZ), isoprene ($34.9 \mu\text{g m}^{-3}$)
 335 ranks 2nd in terms of OFP after formaldehyde ($202.0 \mu\text{g m}^{-3}$), indicating a high impact of biogenic
 336 emissions (Mo et al., 2018; Sindelarova et al., 2014). At the industrial site (XD), the contribution of
 337 isopentane, marker of oil and gas emissions, to OFP is more prominent (as high as $66.2 \mu\text{g m}^{-3}$) than
 338 other sites. OFP of highly reactive aromatic hydrocarbon species, such as m/p- xylene ($53.8 \mu\text{g m}^{-3}$)
 339 ³) and o-xylene ($23.6 \mu\text{g m}^{-3}$) are predominant at upwind site (CQ), indicating outstanding
 340 contribution of solvent-using sources. OFP contributed by alkenes is the highest at urban site
 341 ($101.8 \pm 56.8 \mu\text{g m}^{-3}$) (Figure 5 (a)), with ethylene and propylene being the most key species, which
 342 is consistent with the dense vehicle emission near this site.



343

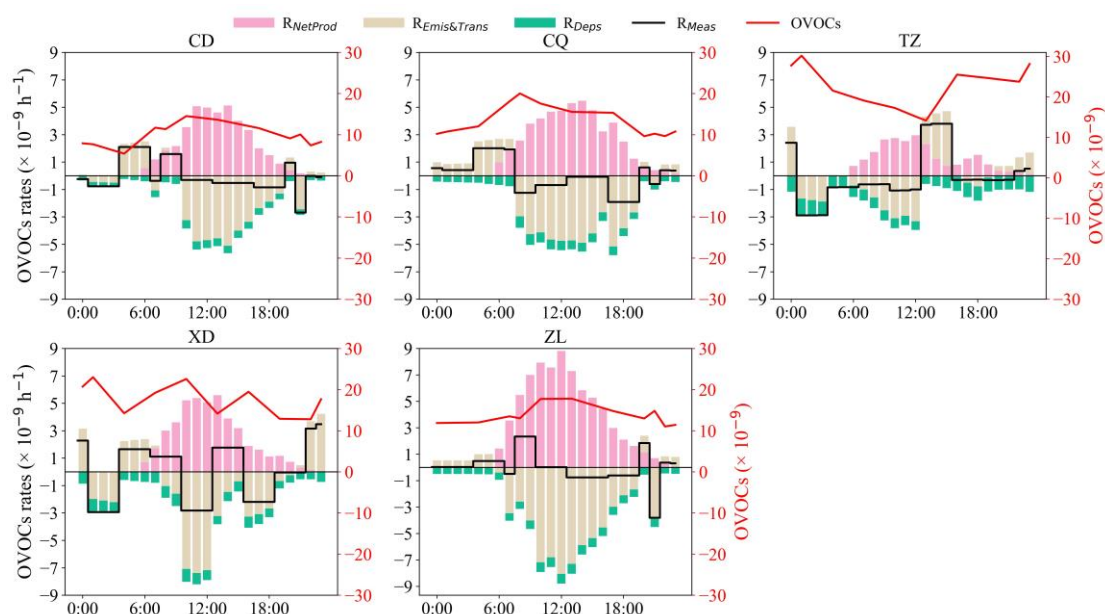
344 **Figure 5. (a) Ozone formation potential (OFP) and (b) proportions of OFP contributed by VOCs subgroups,**
 345 **along with (c) mixing ratios of VOCs subgroups at five sites.**

346 **3.2 Contribution of chemical generation, emissions/transport to OVOCs**

347 OBM simulation results were used to analyze the contributions of chemical processes, and
348 emissions/transport to OVOCs. Overall, the modeled O₃ in the Base scenario exhibited good model
349 performance at the five sites, with R values exceeding 0.85 and IOA values greater than 0.80 (Table
350 S7). These metrics indicate a high level of agreement between observed and modeled data,
351 comparable to results reported in previous studies (Qin et al., 2023; Zheng et al., 2023). The
352 contributions of R_{NetProd} predominantly occur during the daytime (Figure 6). The maximum average
353 daytime R_{NetProd} of OVOCs was observed at ZL ($5.9 \pm 3.5 \times 10^{-9} \text{ h}^{-1}$), followed by CQ ($4.11 \pm 11.9 \times$
354 10^{-9} h^{-1}), XD ($3.6 \pm 2.4 \times 10^{-9} \text{ h}^{-1}$), CD ($3.5 \pm 2.0 \times 10^{-9} \text{ h}^{-1}$) and TZ ($1.9 \pm 3.6 \times 10^{-9} \text{ h}^{-1}$) sites. This
355 suggests that abundant reactive VOCs emissions at urban areas as well as in the industrial areas
356 could lead to faster generation of OVOCs. Generally, the R_{NetProd} varied with a single peak due to
357 photochemical formation and export transport, with the maximum value at 12:00-14:00 LT. The
358 mean peak of R_{NetProd} at ZL was $8.8 \times 10^{-9} \text{ h}^{-1}$, followed by XD ($5.6 \times 10^{-9} \text{ h}^{-1}$), CQ ($5.5 \times 10^{-9} \text{ h}^{-1}$),
359 CD ($5.1 \times 10^{-9} \text{ h}^{-1}$) and TZ ($3.0 \times 10^{-9} \text{ h}^{-1}$). Generally, in the early morning hours (4:00-10:00 LT),
360 positive R_{Meas} at CD, CQ, and XD sites are driven by R_{Emis&Tran} import. During this period, OVOCs
361 mixing ratios show a significant upward trend, peaking between 8:00 and 10:00 LT.

362 Overall, OVOCs mixing ratios at CD, CQ, and ZL sites were typically lower at night but higher
363 during the daytime (Figure 6), attributing to strong daytime photochemical generation, especially at
364 around 7:00-10:00 LT. In contrast, TZ and XD showed higher nighttime OVOCs than that at daytime,
365 which is due to stronger emission import during night. In addition, though R_{NetProd} at ZL was the
366 fastest during the daytime, the air mass transport can efficiently export OVOCs to downwind areas,
367 leading to relatively lower OVOCs mixing ratios. While at TZ, R_{NetProd} was the lowest, but the

368 daytime OVOCs was the highest due to the predominant daytime import, especially the
 369 southwestward import on August 8 (Figure S5 (f)).



370
 371 **Figure 6. Diurnal profiles of OVOCs contributions from local photochemical production (R_{NetProd}),**
 372 **deposition (R_{Dep}), emission/transport ($R_{\text{Emis\&Trans}}$), and measured OVOCs formation rate (R_{Meas}) of the five**
 373 **sites.**

374 3.3 Importance of OVOCs observationally constraint in OBM

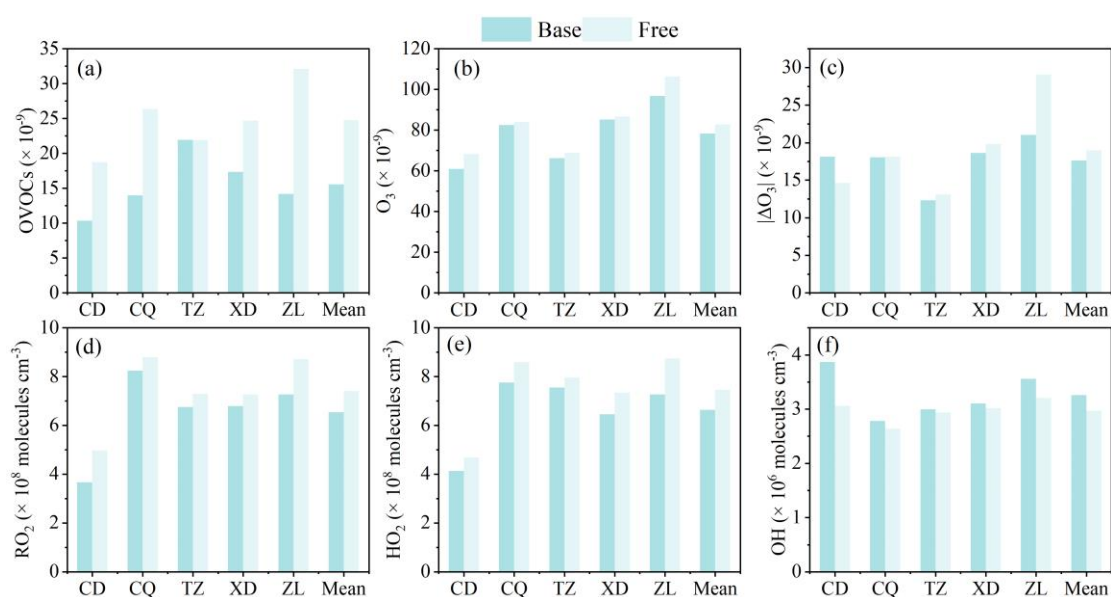
375 To investigate the effect of the constrain setting of OVOCs on OBM performance, the
 376 simulated OVOC, O_3 , radicals in the Free and Base scenarios are compared (Figure 7). It has been
 377 shown that the box model, which did not take into account transport (including horizontal and
 378 vertical diffusion) and emissions, will result in overestimations of OVOCs, peroxy radical and PAN
 379 (Qu et al., 2021). In this study, OVOCs are overestimated by 42.1%~126.5% in the Free scenario
 380 compared with the Base scenario (Figure 7 (a), Figure S6 (c)), especially HCHO (76.3%) and
 381 benzaldehyde (737.5%). The daytime RO_x was overestimated by 6.5%~23.3%, with RO_2 and HO_2
 382 being overestimated by 6.6%~35.1% and 5.3%~20.4%, respectively, while OH was underestimated
 383 by 1.8%~20.9% (Figure 7 (d-f), Figure S7 (b)). As shown in Figure 8 (a), photolysis of OVOCs
 384 (include HCHO) is the predominant source of RO_x radicals ($P(\text{RO}_x)$) in the daytime, which is

385 consistent with the findings in Beijing (Liu et al., 2012), Shanghai (Zhang et al., 2021a), Hong Kong
386 (Xue et al., 2016), and Mexico (Volkamer et al., 2010). To assess the impact of OVOCs on the
387 simulation of RO_x species (RO₂, HO₂, and OH), the chemical budgets of these species, as influenced
388 by OVOCs, are quantified according to Liu et al. (2012) and Xue et al. (2016) (Figure 8 (b), Figure
389 S8 (a)).

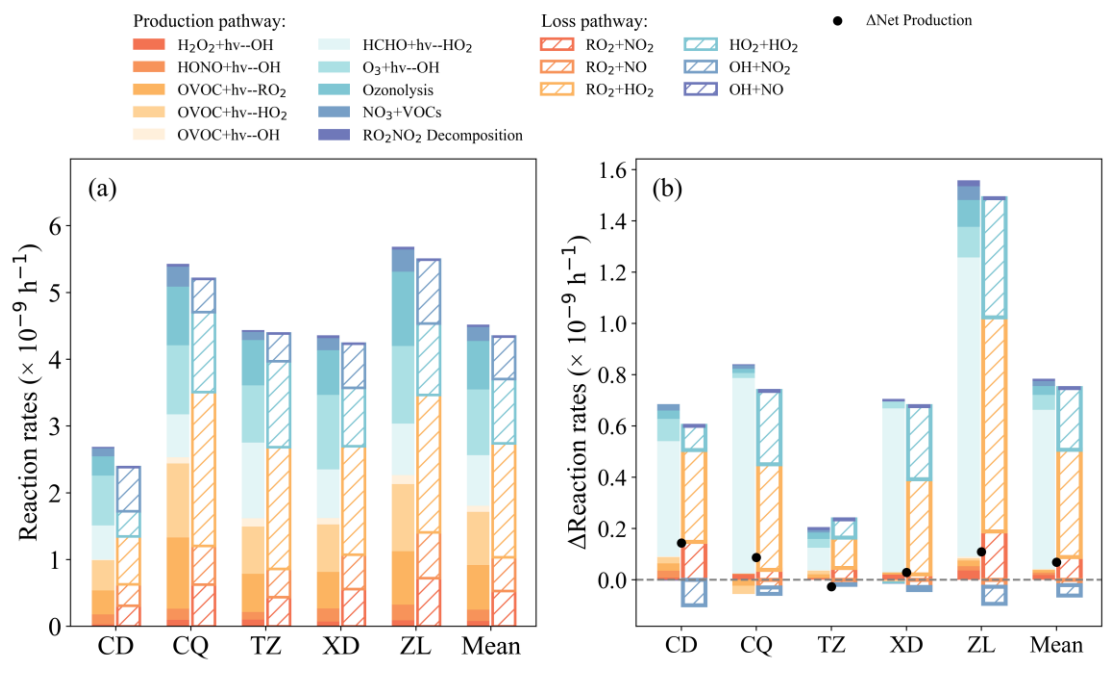
390 In the Free scenario, the daytime net production of RO_x (P(RO_x)) was estimated to range from
391 0.03 to 0.14 × 10⁻⁹ h⁻¹ compared to the Base scenario across four sites (excluding TZ), indicating an
392 overestimation of RO_x. Notably, the TZ site exhibited negative P(RO_x) values, suggesting the
393 potential existence of unaccounted RO_x sources in this region. The mean daytime P(RO_x) in the Free
394 scenario was calculated as 4.8±2.7 × 10⁻⁹ h⁻¹, 18.8% higher than that in the Base scenario (4.0±2.3
395 × 10⁻⁹ h⁻¹). As illustrated in Figure 8 and Figure S8(a), the photolysis of OVOCs (including HCHO)
396 dominates P(RO_x), with a mean rate of 2.9±1.9 × 10⁻⁹ h⁻¹ in the Free scenario, 27.4% higher than
397 that in Base scenario (2.3±1.5 × 10⁻⁹ h⁻¹). This substantial increase in OVOCs photolysis
398 consequently amplified the formation of peroxy radicals (RO₂ and HO₂). Among the production
399 pathways, the photolysis of HCHO demonstrated the most pronounced impact on HO₂ production
400 in the Free scenario (0.1~1.9 × 10⁻⁹ h⁻¹), with an increase of 7.8%~151.2% (0.1~1.2 × 10⁻⁹ h⁻¹) than
401 in the Base scenario (0.5~1.1 × 10⁻⁹ h⁻¹) (Figure 8 (b)).

402 The interference of OVOCs on OH is comprehensive. On the one hand, increased OVOCs
403 tends to elevate the generation of HO₂, which can directly or indirectly boost OH generation via the
404 reaction of NO (Figure S9). On the other hand, the higher OVOCs levels can decrease OH via the
405 reaction of OH+OVOCs (Qu et al., 2021; Tan et al., 2019b). In the Free scenario, total OH sources
406 (including H₂O₂+hv, HONO+hv, O₃+hv, and HO₂+NO) is 7.5~12.1 × 10⁻⁹ h⁻¹, which is 0.3~1.1 ×

407 10^{-9} h^{-1} higher than that in the Base scenario ($10.2\sim 11.0 \times 10^{-9} \text{ h}^{-1}$) (Figure S9). Conversely, OH
 408 destruction to peroxy radicals in the Free scenario ($7.1\sim 11.8 \times 10^{-9} \text{ h}^{-1}$) is $0.3\sim 2.1 \times 10^{-9} \text{ h}^{-1}$ higher
 409 than that in Base scenario ($6.1\sim 9.7 \times 10^{-9} \text{ h}^{-1}$), leading to a net OH loss of $0.1\sim 0.9 \times 10^{-9} \text{ h}^{-1}$. This
 410 underestimation of OH without OVOCs constraint biases atmospheric oxidation capacity (AOC) by
 411 0.1%~10.0% (excluding XD) (Figure S10), affecting the evaluation of VOCs decay via OH
 412 oxidation (Li et al., 2022).

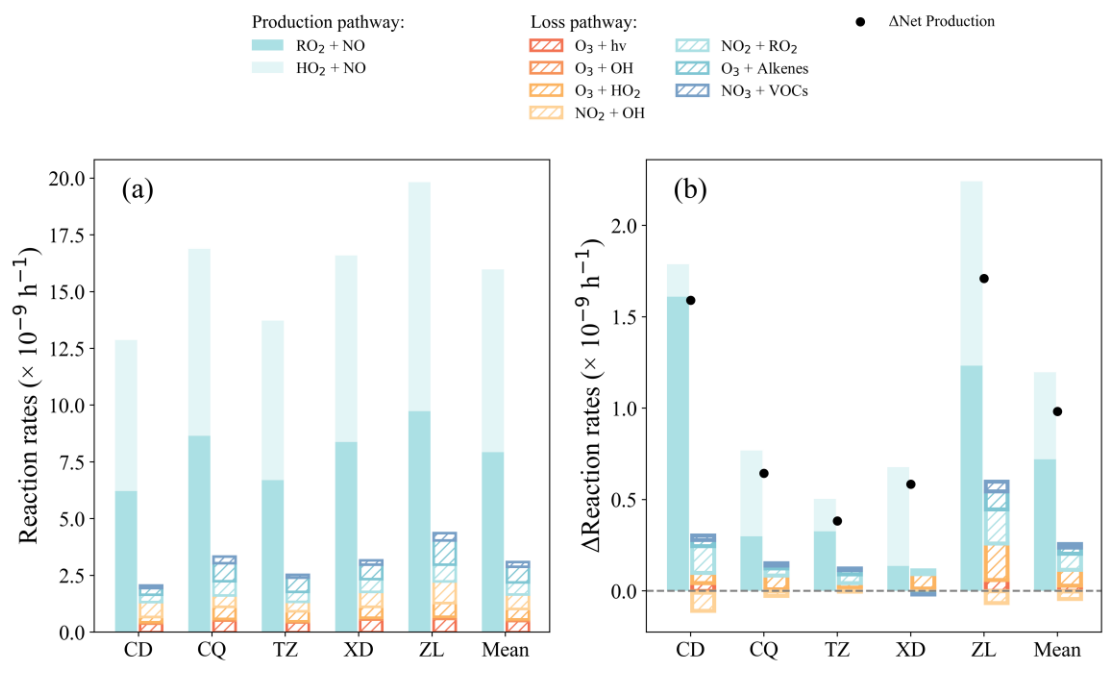


413
 414 **Figure 7. Comparison of average (a) OVOC, (b) daytime O_3 , (c) daytime $|\Delta\text{O}_3|$ (the gap between simulated**
 415 **and observed daytime (8:00-18:00 LT) O_3 mixing ratios), and RO_x ((d) RO_2 , (e) HO_2 , and (f) OH) between**
 416 **the Base and Free scenario simulations.**



417
418
419
420

Figure 8. (a) Average daytime (8:00-18:00 LT) sources and sinks of RO_x in Base case and (b) the impact of OVOCs observational constraints on RO_x budget, calculated by the difference between the Free and Base scenarios.



421
422
423
424

Figure 9. (a) Average daytime (8:00-18:00 LT) O₃ production and loss rates (× 10⁻⁹ h⁻¹) in Base scenario and (b) the impact of OVOCs observational constraints on O₃ budget, calculated by the difference between the Free and Base scenarios.

425 Overall, the gap between simulated and observed daytime O₃ mixing ratios ($|\Delta O_3|$) in the Free
426 case increased by 7.5% compared to that in the Base scenario. To better understand the influence of

427 OVOCs on O₃ formation, the rates of the main production and sink pathways of O₃ in the Base and
428 Free scenarios are summarized (Figure 9, Figure S8 (b)). Compared to the Base scenario, the diurnal
429 P(O₃) in the Free scenario increases by 3.7%~13.9%, with the reaction rates of RO₂+NO and
430 HO₂+NO increases by 1.6%~25.9% ($0.1\sim1.6 \times 10^{-9} \text{ h}^{-1}$) and 2.5%~10.0% ($0.2\sim1.0 \times 10^{-9} \text{ h}^{-1}$),
431 respectively. This is attributed to the elevated RO₂ and HO₂ radical concentrations simulated without
432 constraints of OVOCs observations (Figure 7 (d-e)). In contrast, the lower simulated concentration
433 of OH radicals in the Free scenario results in a 0.5%~14.8% ($0\sim0.1 \times 10^{-9} \text{ h}^{-1}$) decrease in the
434 OH+O₃/NO₂ reaction rate. Although the L(O₃) in the Free scenario is $0.4\sim1.7 \times 10^{-9} \text{ h}^{-1}$ higher than
435 that in the Base scenario, it cannot offset the increase of P(O₃), leading to higher net product of O₃.
436 Thus, no constraints of OVOCs could lead to overestimate peroxy radicals in the OBM, which in
437 turn significantly overestimates the deviation of O₃ due to the formation pathway of RO₂/HO₂+NO.
438 Of course, the impact of OVOCs varies considerably in different emission and functional regions.
439 The simulated mean daytime O₃ in the Free scenario is 106.3, 86.7, 84.1, 68.8, and $68.2 \times 10^{-9} \text{ h}^{-1}$
440 at ZL, XD, CQ, TZ, and CD, respectively, which is 9.8%, 1.8%, 2.0%, 3.9%, and 11.9% higher than
441 that in the Base scenario (Figure 7 (b), Table S8). The mean diurnal $|\Delta\text{O}_3|$ at ZL site (29.1×10^{-9} ,
442 38.2%) in the Free scenario was significantly higher compared to that of the Base scenario, followed
443 by XD (19.8×10^{-9} , 6.4%), TZ (13.1×10^{-9} , 6.2%) and CQ (18.1×10^{-9} , 0.6%) (Figure 7 (c), Table
444 S8), suggesting that the absence of OVOCs constraint in OBM can significantly bias the O₃
445 formation analysis in urban and industrial areas with complex emissions.

446 **3.4 Uncertainty analysis**

447 The uncertainty of the model mainly comes from the setting of NO_x (Text S1). Sensitive model
448 runs are performed with different NO_x settings to show the corresponding uncertainty. Firstly, NO_{ss},

449 VOCs, OVOCs, T, RH, and BLH are constrained by the observed data, and sensitivity simulations
450 were carried out for gradient NO₂ mixing ratios (50%, 60%, 70%, and 100% of observed NO₂
451 mixing ratios). At the four sites (except TZ), different NO₂ settings produce uncertainties of -
452 12%~25% for daytime O₃ and -17%~36% for the daytime R_{NetProd} of OVOCs. In addition, different
453 NO₂ settings produce uncertainties of -27%~51% for the R_{Emiss&Trans} of OVOCs. This indicates that
454 reducing the uncertainty of NO₂ observations is important for further atmospheric chemistry
455 modelling. Secondly, the NO_{ss} and observed NO mixing ratio was respectively used in the model to
456 investigate the influence of nearby NO emissions on the OBM result (Table S3). Sensitivity tests
457 show that directly using the observed NO data may result in an uncertainty of 3% ~20%, 10%
458 ~27% and 7.1%~38% for O₃, R_{NetProd} and R_{Emiss&Trans}, respectively, with significantly higher
459 uncertainties at TZ than at other stations, which may be related to the strong transient emissions of
460 NO_x.

461 The OH radicals are the main oxidant in the atmospheric troposphere. Most trace gases (CO,
462 CH₄ and VOCs) react with OH to produce peroxy radicals, including HO₂, and RO₂. Peroxy
463 radicals then react with NO to promote O₃. Photolysis of HONO is one of the important sources of
464 OH radicals. However, direct measurement of HONO was not conducted in this study. The input of
465 HONO in this study used the value of linear relationship with NO₂ mixing ratios, which may cause
466 some uncertainty. Sensitivity analyses were conducted based on the typical urban site (ZL) to
467 quantify the effect of different HONO/NO₂ ratios on free radicals and O₃. As shown in Figure S12,
468 as the ratio of HONO/NO₂ increased, the mixing ratio of HONO increased, and the concentration
469 of OH produced by photolysis of HONO increased. At the same time, the peroxy radical and O₃
470 concentrations also increased (Table S9). At the lowest HONO/NO₂ ratio (0.005), the daytime OH,

471 HO₂, RO₂, and O₃ levels decreased by 4.6%, 4.8%, 6.0%, and 3.4%, respectively, compared to the
472 HONO/NO₂ ratio of 0.02. On the contrary, at the highest HONO/NO₂ of 0.04, the daytime OH, HO₂,
473 RO₂, and O₃ levels increased by 5.4%, 5.6%, 7.2% and 3.8%, respectively, compared to the Base
474 case.

475 When analyzing the contribution of chemical pathways, emission/transport and deposition to
476 OVOCs according to Equations (1-3), the OVOC budget may be affected by the modeling time step.
477 A sensitivity analysis was conducted at ZL, with simulations at different time steps (30 min, 10 min,
478 and 5 min). As shown in Figure S13, the diurnal trends of the chemical contributions (R_{NetProd}),
479 emission/transport ($R_{\text{Emis\&Trans}}$) and deposition (R_{Deps}) to OVOC are similar. The magnitude of the
480 instantaneous change in $R_{\text{Emis\&Trans}}$ decreases when the time step is shortened. Specifically, the
481 contributions of R_{NetProd} and $R_{\text{Emis\&Trans}}$ to OVOC increased, while the contribution of R_{Deps}
482 decreased with shorter time steps (Table S10). When the time step was reduced to 5 minutes, the
483 contributions of R_{NetProd} and $R_{\text{Emis\&Trans}}$ to OVOC increased by 4.3% and 5.0%, respectively, while
484 the contribution of R_{Deps} decreased by 0.2%. Therefore, shortening the time step in the model
485 simulation may result in limited increase contribution from R_{NetProd} and $R_{\text{Emis\&Trans}}$ to OVOC.

486 The OBM, while advantageous for its use of the near-explicit master chemical mechanism and
487 its ability to reproduce atmospheric chemistry based on observations, has several inherent
488 limitations. Firstly, it inadequately considers emission and transport processes (Wolfe et al., 2016),
489 leading to uncertainties and potential biases in atmospheric chemical analysis. Future studies could
490 differentiate the two processes using CTMs. Secondly, the steady-state assumption, which underpins
491 OBM calculations, might become invalid in areas strongly influenced by nearby emissions (e.g.,
492 high-traffic and industrial intensive regions) (Wolfe et al., 2016). This may potentially cause

493 overestimations of secondary products such as O₃, RO_x radicals, and OVOCs (Li et al., 2021, 2014b).
494 In this study, simulations use NO_{ss} as inputs, acknowledging that traffic-related NO emissions may
495 prevent the system from reaching an approximate steady state. The associated uncertainties have
496 been discussed above. Lastly, the model may not fully capture all relevant chemical processes, such
497 as heterogeneous reactions or the formation and the fate of intermediate species. For instance, the
498 exclusion of ClNO₂ chemistry could result in underestimating RO_x and O₃ production in certain
499 environments (Riedel et al., 2014; Xia et al., 2020). Future research should focus on refining the
500 chemical mechanisms to better approximate real atmospheric conditions.

501 **4. Conclusions**

502 Compared with previous studies conducted in most Chinese cities, the VOCs level in Zibo is
503 in the upper-middle range ($>32 \times 10^{-9}$), with OVOCs being the second-largest contributor
504 (29.4%~36.1%) after alkanes (34.8%~53.3%). Higher levels of OVOCs were observed at sites with
505 more prominent emissions, with mixing ratios ranked as suburban (TZ, 19.7×10^{-9}) > industrial
506 (XD, 16.8×10^{-9}) > urban (ZL, 14.9×10^{-9}) > upwind (CQ, 13.9×10^{-9}) > downwind (CD, $10.4 \times$
507 10^{-9}). The OFP in Zibo is $410.4 \pm 197.2 \mu\text{g m}^{-3}$, with OVOCs accounting for the largest proportion
508 (31.5%~55.9%). The upwind site (CQ, $464.2 \pm 162.3 \mu\text{g m}^{-3}$) has the highest OFP, followed by the
509 suburban site (TZ, $456.3 \pm 295.3 \mu\text{g m}^{-3}$), the urban site (ZL, $441.1 \pm 174.5 \mu\text{g m}^{-3}$), the industrial site
510 (XD, $422.9 \pm 166.9 \mu\text{g m}^{-3}$), and the downwind site (CD, $279.4 \pm 101.2 \mu\text{g m}^{-3}$) (Table S5). OFP
511 contributed by OVOCs is most dominant at suburban (TZ, $254.9 \mu\text{g m}^{-3}$) and industrial (XD, 194.7
512 $\mu\text{g m}^{-3}$) sites, followed by urban (ZL, $148.9 \mu\text{g m}^{-3}$), upwind (CQ, $146.2 \mu\text{g m}^{-3}$), and downwind
513 (CD, $102.3 \mu\text{g m}^{-3}$) sites. The high levels of OVOCs and their significant contribution to OFP
514 highlights their crucial role in O₃ production across the observing stations.

515 Based on the OBM simulation, daytime OVOCs primarily originate from photochemical
516 generation, while at nighttime, emissions/transport is the main sources. This diurnal pattern is
517 closely related to the cyclical nature of human activities in urban areas (ZL), where stronger human
518 activities such as vehicle emissions in the daytime enhance the secondary generation of OVOCs.
519 Conversely, in industrial and suburban areas (XD, CQ, and TZ), emissions/transports dominate
520 nighttime OVOC levels, leading to higher mixing ratios at night compared to the daytime.

521 Without OVOCs constraint in the OBM, OVOCs are overestimated by 42.1%~126.5% in the
522 Free scenario. The impact of OVOCs constraint on P(RO_x) is most significant at the urban site (ZL)
523 (29.4%), comparable to downwind site (CD) (27.6%), and higher than the industrial site (XD)
524 (17.8%), upwind site (CQ) (15.8%) and suburban site (TZ) (4.7%). In addition, this overestimation
525 of OVOCs in the Free scenario accelerates the reaction of OH with OVOCs and the photolysis of
526 OVOCs, promoting increased production of RO₂ (6.6%~35.1%) and HO₂ (5.3%~ 20.4%), which in
527 turn leads to an overestimation of O₃ (1.8%~11.9%) during the daytime. However, the reaction rates
528 of OH with OVOCs are overestimated without OVOCs constraint, which leads to underestimation
529 of OH (3.4%~12.7%) and AOC (0.1%~10.0%). Therefore, to minimize the bias of numerical models,
530 particularly in areas with complex anthropogenic activities, it is essential to intensify OVOCs
531 observations and integrate them into numerical models. These efforts are crucial for refining
532 atmospheric photochemistry simulation, improving the accuracy of O₃ formation predictions, and
533 formulating more effective air quality management strategies for regions experiencing similar
534 pollution challenges.

535 **Author contributions**

536 KZ, XY, RL, JX, QL, LSS, JQL, YNY, FTW and LMY conducted the field measurements.

537 JWD and KZ performed the data analysis and prepared the manuscript with contributions from all
538 co-authors. KZ, YLF, HC, LH, JNT, YJW and LL reviewed and edited the manuscript. All authors
539 contributed to data interpretation and discussions.

540 **Data availability**

541 The model output is available upon request by contacting the corresponding author.

542 **Author contributions**

543 LL conceptualized this study along with ZK. YX, LR, XJ, LQ, SLS, LJQ, YYN, WFT and YLM did
544 the field observation. Data analysis and model simulation were done by ZK and DJW. The
545 manuscript draft was prepared by DJW, and editing was done by ZK, LL, FYL, CH, HL, TJN and
546 WYJ.

547

548 **Competing interests**

549 The contact author has declared that none of the authors has any competing interests.

550 **Acknowledgment**

551 This study was financially supported by the National research program for key issues in air
552 pollution control (DQGG202119). This work is supported by Shanghai Technical Service Center of
553 Science and Engineering Computing, Shanghai University.

554 **References**

- 555 Armstrong, R. A., Slade, S. V., and Eperjesi, F.: An introduction to analysis of variance (ANOVA)
556 with special reference to data from clinical experiments in optometry, *Ophthalmic and*
557 *Physiological Optics*, 20, 235–241, <https://doi.org/10.1046/j.1475-1313.2000.00502.x>, 2000.
- 558 Atkinson, R.: Atmospheric chemistry of VOCs and NO_x, *Atmos. Environ.*, 34, 2063–2101,
559 [https://doi.org/10.1016/S1352-2310\(99\)00460-4](https://doi.org/10.1016/S1352-2310(99)00460-4), 2000.
- 560 Atkinson, R. and Arey, J.: Atmospheric Degradation of Volatile Organic Compounds, *Chem. Rev.*,
561 103, 4605–4638, <https://doi.org/10.1021/cr0206420>, 2003.
- 562 Bufalini, J. J. and Dodge, M. C.: Ozone-forming potential of light saturated hydrocarbons, *Environ.*

563 Sci. Technol., 17, 308–311, <https://doi.org/10.1021/es00111a013>, 1983.

564 Carter, W.: Updated maximum incremental reactivity scale and hydrocarbon bin reactivities for
565 regulatory applications, California Air Resources Board Contract, 1, 07–339, 2010a.

566 Carter, W. P. L.: A detailed mechanism for the gas-phase atmospheric reactions of organic
567 compounds, *Atmospheric Environment. Part A. General Topics*, 24, 481–518,
568 [https://doi.org/10.1016/0960-1686\(90\)90005-8](https://doi.org/10.1016/0960-1686(90)90005-8), 1990.

569 Carter, W. P. L.: Development of the SAPRC-07 chemical mechanism, *Atmos. Environ.*, 44, 5324–
570 5335, <https://doi.org/10.1016/j.atmosenv.2010.01.026>, 2010b.

571 Carter, W. P. L. and Heo, G.: Development of revised SAPRC aromatics mechanisms, *Atmos.*
572 *Environ.*, 77, 404–414, <https://doi.org/10.1016/j.atmosenv.2013.05.021>, 2013.

573 Chen, T., Xue, L., Zheng, P., Zhang, Y., Liu, Y., Sun, J., Han, G., Li, H., Zhang, X., Li, Y., Li, H.,
574 Dong, C., Xu, F., Zhang, Q., and Wang, W.: Volatile organic compounds and ozone air pollution
575 in an oil production region in northern China, *Atmos. Chem. Phys.*, 20, 7069–7086,
576 <https://doi.org/10.5194/acp-20-7069-2020>, 2020.

577 Chen, T., Zheng, P., Zhang, Y., Dong, C., Han, G., Li, H., Yang, X., Liu, Y., Sun, J., Li, H., Zhang,
578 X., Li, Y., Wang, W., and Xue, L.: Characteristics and formation mechanisms of atmospheric
579 carbonyls in an oilfield region of northern China, *Atmos. Environ.*, 274, 118958,
580 <https://doi.org/10.1016/j.atmosenv.2022.118958>, 2022.

581 Del Negro, L. A., Fahey, D. W., Gao, R. S., Donnelly, S. G., Keim, E. R., Neuman, J. A., Cohen, R.
582 C., Perkins, K. K., Koch, L. C., Salawitch, R. J., Lloyd, S. A., Proffitt, M. H., Margitan, J. J.,
583 Stimpfle, R. M., Bonne, G. P., Voss, P. B., Wennberg, P. O., McElroy, C. T., Swartz, W. H.,
584 Kusterer, T. L., Anderson, D. E., Lait, L. R., and Bui, T. P.: Comparison of modeled and observed
585 values of NO₂ and JNO₂ during the Photochemistry of Ozone Loss in the Arctic Region in
586 Summer (POLARIS) mission, *J. Geophys. Res.-Atmos.*, 104, 26687–26703,
587 <https://doi.org/10.1029/1999JD900246>, 1999.

588 Duan, J., Tan, J., Yang, L., Wu, S., and Hao, J.: Concentration, sources and ozone formation potential
589 of volatile organic compounds (VOCs) during ozone episode in Beijing, *Atmospheric Research*,
590 88, 25–35, <https://doi.org/10.1016/j.atmosres.2007.09.004>, 2008.

591 Edwards, P. M., Brown, S. S., Roberts, J. M., Ahmadov, R., Banta, R. M., deGouw, J. A., Dube, W.
592 P., Field, R. A., Flynn, J. H., Gilman, J. B., Graus, M., Helmig, D., Koss, A., Langford, A. O.,
593 Lefer, B. L., Lerner, B. M., Li, R., Li, S.-M., McKeen, S. A., Murphy, S. M., Parrish, D. D., Senff,
594 C. J., Soltis, J., Stutz, J., Sweeney, C., Thompson, C. R., Trainer, M. K., Tsai, C., Veres, P. R.,
595 Washenfelder, R. A., Warneke, C., Wild, R. J., Young, C. J., Yuan, B., and Zamora, R.: High
596 winter ozone pollution from carbonyl photolysis in an oil and gas basin, *Nature*, 514, 351–354,
597 <https://doi.org/10.1038/nature13767>, 2014.

598 Elshorbany, Y. F., Kurtenbach, R., Wiesen, P., Lissi, E., Rubio, M., Villena, G., Gramsch, E., Rickard,
599 A. R., Pilling, M. J., and Kleffmann, J.: Oxidation capacity of the city air of Santiago, Chile,
600 *Atmos. Chem. Phys.*, 9, 2257–2273, <https://doi.org/10.5194/acp-9-2257-2009>, 2009.

601 Elshorbany, Y. F., Steil, B., Bruehl, C., and Lelieveld, J.: Impact of HONO on global atmospheric
602 chemistry calculated with an empirical parameterization in the EMAC model, *Atmos. Chem.*
603 *Phys.*, 12, 9977–10000, <https://doi.org/10.5194/acp-12-9977-2012>, 2012.

604 Emmerson, K. M., Carslaw, N., and Pilling, M. J.: Urban atmospheric chemistry during the PUMA
605 campaign 2: Radical budgets for OH, HO₂ and RO₂, *J. Atmos. Chem.*, 52, 165–183,
606 <https://doi.org/10.1007/s10874-005-1323-2>, 2005.

607 Fuchs, H., Tan, Z., Lu, K., Bohn, B., Broch, S., Brown, S. S., Dong, H., Gomm, S., Häsel, R., He,
608 L., Hofzumahaus, A., Holland, F., Li, X., Liu, Y., Lu, S., Min, K.-E., Rohrer, F., Shao, M., Wang,
609 B., Wang, M., Wu, Y., Zeng, L., Zhang, Y., Wahner, A., and Zhang, Y.: OH reactivity at a rural
610 site (Wangdu) in the North China Plain: contributions from OH reactants and experimental OH
611 budget, *Atmos. Chem. Phys.*, 17, 645–661, <https://doi.org/10.5194/acp-17-645-2017>, 2017.

612 Gentner, D. R., Worton, D. R., Isaacman, G., Davis, L. C., Dallmann, T. R., Wood, E. C., Herndon,
613 S. C., Goldstein, A. H., and Harley, R. A.: Chemical Composition of Gas-Phase Organic Carbon
614 Emissions from Motor Vehicles and Implications for Ozone Production, *Environ. Sci. Technol.*,
615 47, 11837–11848, <https://doi.org/10.1021/es401470e>, 2013.

616 Geyer, A., Aliche, B., Konrad, S., Schmitz, T., Stutz, J., and Platt, U.: Chemistry and oxidation
617 capacity of the nitrate radical in the continental boundary layer near Berlin, *J. Geophys. Res.-*
618 *Atmos.*, 106, 8013–8025, <https://doi.org/10.1029/2000JD900681>, 2001.

619 Gilman, J. B., Lerner, B. M., Kuster, W. C., Goldan, P. D., Warneke, C., Veres, P. R., Roberts, J. M.,
620 de Gouw, J. A., Burling, I. R., and Yokelson, R. J.: Biomass burning emissions and potential air
621 quality impacts of volatile organic compounds and other trace gases from fuels common in the
622 US, *Atmos. Chem. Phys.*, 15, 13915–13938, <https://doi.org/10.5194/acp-15-13915-2015>, 2015.

623 Goldan, P. D., Kuster, W. C., Williams, E., Murphy, P. C., Fehsenfeld, F. C., and Meagher, J.:
624 Nonmethane hydrocarbon and oxy hydrocarbon measurements during the 2002 New England Air
625 Quality Study, *J. Geophys. Res.-Atmos.*, 109, D21309, <https://doi.org/10.1029/2003JD004455>,
626 2004.

627 Goliff, W. S., Stockwell, W. R., and Lawson, C. V.: The regional atmospheric chemistry mechanism,
628 version 2, *Atmos. Environ.*, 68, 174–185, <https://doi.org/10.1016/j.atmosenv.2012.11.038>, 2013.

629 de Gouw, J. A., Gilman, J. B., Kim, S.-W., Alvarez, S. L., Dusanter, S., Graus, M., Griffith, S. M.,
630 Isaacman-VanWertz, G., Kuster, W. C., Lefer, B. L., Lerner, B. M., McDonald, B. C.,
631 Rappenglück, B., Roberts, J. M., Stevens, P. S., Stutz, J., Thalman, R., Veres, P. R., Volkamer, R.,
632 Warneke, C., Washenfelder, R. A., and Young, C. J.: Chemistry of Volatile Organic Compounds
633 in the Los Angeles Basin: Formation of Oxygenated Compounds and Determination of Emission
634 Ratios, *Journal of Geophysical Research: Atmospheres*, 123, 2298–2319,
635 <https://doi.org/10.1002/2017JD027976>, 2018.

636 Guo, F., Bui, A. A. T., Schulze, B. C., Yoon, S., Shrestha, S., Wallace, H. W., Sakai, Y., Actkinson,
637 B. W., Erickson, M. H., Alvarez, S., Sheesley, R., Usenko, S., Flynn, J., and Griffin, R. J.: Urban
638 core-downwind differences and relationships related to ozone production in a major urban area
639 in Texas, *Atmos. Environ.*, 262, 118624, <https://doi.org/10.1016/j.atmosenv.2021.118624>, 2021.

640 Han, Y., Huang, X., Wang, C., Zhu, B., and He, L.: Characterizing oxygenated volatile organic
641 compounds and their sources in rural atmospheres in China, *J. Environ. Sci.*, 81, 148–155,
642 <https://doi.org/10.1016/j.jes.2019.01.017>, 2019.

643 Huang, X.-F., Zhang, B., Xia, S.-Y., Han, Y., Wang, C., Yu, G.-H., and Feng, N.: Sources of
644 oxygenated volatile organic compounds (OVOCs) in urban atmospheres in North and South
645 China, *Environ. Pollut.*, 261, 114152, <https://doi.org/10.1016/j.envpol.2020.114152>, 2020.

646 Jenkin, M. E., Young, J. C., and Rickard, A. R.: The MCM v3.3.1 degradation scheme for isoprene,
647 *Atmos. Chem. Phys.*, 15, 11433–11459, <https://doi.org/10.5194/acp-15-11433-2015>, 2015.

648 Jiang, P., Chen, X., Li, Q., Mo, H., and Li, L.: High-resolution emission inventory of gaseous and
649 particulate pollutants in Shandong Province, eastern China, *Journal of Cleaner Production*, 259,
650 120806, <https://doi.org/10.1016/j.jclepro.2020.120806>, 2020.

651 Kanaya, Y., Pochanart, P., Liu, Y., Li, J., Tanimoto, H., Kato, S., Suthawaree, J., Inomata, S.,
652 Taketani, F., Okuzawa, K., Kawamura, K., Akimoto, H., and Wang, Z. F.: Rates and regimes of
653 photochemical ozone production over Central East China in June 2006: a box model analysis
654 using comprehensive measurements of ozone precursors, *Atmos. Chem. Phys.*, 9, 7711–7723,
655 <https://doi.org/10.5194/acp-9-7711-2009>, 2009.

656 Karl, T., Striednig, M., Graus, M., Hammerle, A., and Wohlfahrt, G.: Urban flux measurements
657 reveal a large pool of oxygenated volatile organic compound emissions, *Proc. Natl. Acad. Sci. U.*
658 *S. A.*, 115, 1186–1191, <https://doi.org/10.1073/pnas.1714715115>, 2018.

659 Karl, T. G., Christian, T. J., Yokelson, R. J., Artaxo, P., Hao, W. M., and Guenther, A.: The Tropical
660 Forest and Fire Emissions Experiment: method evaluation of volatile organic compound
661 emissions measured by PTR-MS, FTIR, and GC from tropical biomass burning, *Atmos. Chem.*
662 *Phys.*, 7, 5883–5897, <https://doi.org/10.5194/acp-7-5883-2007>, 2007.

663 Kim, S., Kim, S.-Y., Lee, M., Shim, H., Wolfe, G. M., Guenther, A. B., He, A., Hong, Y., and Han,
664 J.: Impact of isoprene and HONO chemistry on ozone and OVOC formation in a semirural South
665 Korean forest, *Atmos. Chem. Phys.*, 15, 4357–4371, <https://doi.org/10.5194/acp-15-4357-2015>,
666 2015.

667 Koss, A. R., de Gouw, J., Warneke, C., Gilman, J. B., Lerner, B. M., Graus, M., Yuan, B., Edwards,
668 P., Brown, S. S., Wild, R., Roberts, J. M., Bates, T. S., and Quinn, P. K.: Photochemical aging of
669 volatile organic compounds associated with oil and natural gas extraction in the Uintah Basin,
670 UT, during a wintertime ozone formation event, *Atmos. Chem. Phys.*, 15, 5727–5741,
671 <https://doi.org/10.5194/acp-15-5727-2015>, 2015.

672 Legreid, G., Reimann, S., Steinbacher, M., Staehelin, J., Young, D., and Stemmler, K.:
673 Measurements of OVOCs and NMHCs in a swiss highway tunnel for estimation of road transport
674 emissions, *Environ. Sci. Technol.*, 41, 7060–7066, <https://doi.org/10.1021/es062309+>, 2007.

675 Li, B., Yu, S., Shao, M., Li, X., Ho, S. S. H., Hu, X., Wang, H., Feng, R., and Fang, X.: New insights
676 into photochemical initial concentrations of VOCs and their source implications, *Atmos. Environ.*,
677 298, 119616, <https://doi.org/10.1016/j.atmosenv.2023.119616>, 2023.

678 Li, C., Liu, Y., Cheng, B., Zhang, Y., Liu, X., Qu, Y., An, J., Kong, L., Zhang, Y., Zhang, C., Tan,
679 Q., and Feng, M.: A comprehensive investigation on volatile organic compounds (VOCs) in 2018
680 in Beijing, China: Characteristics, sources and behaviours in response to O₃ formation, *Sci. Total*
681 *Environ.*, 806, 150247, <https://doi.org/10.1016/j.scitotenv.2021.150247>, 2022a.

682 Li, H., Ma, Y., Duan, F., He, K., Zhu, L., Huang, T., Kimoto, T., Ma, X., Ma, T., Xu, L., Xu, B.,
683 Yang, S., Ye, S., Sun, Z., An, J., and Zhang, Z.: Typical winter haze pollution in Zibo, an industrial
684 city in China: Characteristics, secondary formation, and regional contribution, *Environmental*
685 *Pollution*, 229, 339–349, <https://doi.org/10.1016/j.envpol.2017.05.081>, 2017.

686 Li, J., Xie, X., Li, L., Wang, X., Wang, H., Jing, S., Ying, Q., Qin, M., and Hu, J.: Fate of Oxygenated
687 Volatile Organic Compounds in the Yangtze River Delta Region: Source Contributions and
688 Impacts on the Atmospheric Oxidation Capacity, *Environ. Sci. Technol.*, 56, 11212–11224,
689 <https://doi.org/10.1021/acs.est.2c00038>, 2022b.

690 Li, K., Wang, X., Li, L., Wang, J., Liu, Y., Cheng, X., Xu, B., Wang, X., Yan, P., Li, S., Geng, C.,
691 Yang, W., Azzi, M., and Bai, Z.: Large variability of O₃-precursor relationship during severe
692 ozone polluted period in an industry-driven cluster city (Zibo) of North China Plain, *J. Clean*
693 *Prod.*, 316, 128252, <https://doi.org/10.1016/j.jclepro.2021.128252>, 2021a.

694 Li, K., Jacob, D. J., Liao, H., Qiu, Y., Shen, L., Zhai, S., Bates, K. H., Sulprizio, M. P., Song, S., Lu,

695 X., Zhang, Q., Zheng, B., Zhang, Y., Zhang, J., Lee, H. C., and Kuk, S. K.: Ozone pollution in
696 the North China Plain spreading into the late-winter haze season, *Proc. Natl. Acad. Sci. U. S. A.*,
697 118, e2015797118, <https://doi.org/10.1073/pnas.2015797118>, 2021b.

698 Li, L., Chen, Y., Zeng, L., Shao, M., Xie, S., Chen, W., Lu, S., Wu, Y., and Cao, W.: Biomass burning
699 contribution to ambient volatile organic compounds (VOCs) in the Chengdu-Chongqing Region
700 (CCR), China, *Atmos. Environ.*, 99, 403–410, <https://doi.org/10.1016/j.atmosenv.2014.09.067>,
701 2014a.

702 Li, M., Zhang, Q., Streets, D. G., He, K. B., Cheng, Y. F., Emmons, L. K., Huo, H., Kang, S. C., Lu,
703 Z., Shao, M., Su, H., Yu, X., and Zhang, Y.: Mapping Asian anthropogenic emissions of non-
704 methane volatile organic compounds to multiple chemical mechanisms, *Atmos. Chem. Phys.*, 14,
705 5617–5638, <https://doi.org/10.5194/acp-14-5617-2014>, 2014b.

706 Li, M., Zhang, Q., Zheng, B., Tong, D., Lei, Y., Liu, F., Hong, C., Kang, S., Yan, L., Zhang, Y., Bo,
707 Y., Su, H., Cheng, Y., and He, K.: Persistent growth of anthropogenic non-methane volatile
708 organic compound (NMVOC) emissions in China during 1990-2017: drivers, speciation and
709 ozone formation potential, *Atmos. Chem. Phys.*, 19, 8897–8913, <https://doi.org/10.5194/acp-19-8897-2019>, 2019.

711 Li, X., Rohrer, F., Brauers, T., Hofzumahaus, A., Lu, K., Shao, M., Zhang, Y. H., and Wahner, A.:
712 Modeling of HCHO and CHOCHO at a semi-rural site in southern China during the PRIDE-
713 PRD2006 campaign, *Atmos. Chem. Phys.*, 14, 12291–12305, <https://doi.org/10.5194/acp-14-12291-2014>, 2014c.

715 Ling, Z. H., Guo, H., Lam, S. H. M., Saunders, S. M., and Wang, T.: Atmospheric photochemical
716 reactivity and ozone production at two sites in Hong Kong: Application of a Master Chemical
717 Mechanism–photochemical box model, *J. Geophys. Res.-Atmos.*, 119, 10567–10582,
718 <https://doi.org/10.1002/2014JD021794>, 2014.

719 Liu, G., Ma, X., Li, W., Chen, J., Ji, Y., and An, T.: Pollution characteristics, source appointment
720 and environmental effect of oxygenated volatile organic compounds in Guangdong-Hong Kong-
721 Macao Greater Bay Area: Implication for air quality management, *Sci. Total Environ.*, 919,
722 170836, <https://doi.org/10.1016/j.scitotenv.2024.170836>, 2024.

723 Liu, T., Hong, Y., Li, M., Xu, L., Chen, J., Bian, Y., Yang, C., Dan, Y., Zhang, Y., Xue, L., Zhao, M.,
724 Huang, Z., and Wang, H.: Atmospheric oxidation capacity and ozone pollution mechanism in a
725 coastal city of southeastern China: analysis of a typical photochemical episode by an observation-
726 based model, *Atmos. Chem. Phys.*, 22, 2173–2190, <https://doi.org/10.5194/acp-22-2173-2022>,
727 2022.

728 Liu, Y., Yuan, B., Li, X., Shao, M., Lu, S., Li, Y., Chang, C.-C., Wang, Z., Hu, W., Huang, X., He,
729 L., Zeng, L., Hu, M., and Zhu, T.: Impact of pollution controls in Beijing on atmospheric
730 oxygenated volatile organic compounds (OVOCs) during the 2008 Olympic Games: observation
731 and modeling implications, *Atmos. Chem. Phys.*, 15, 3045–3062, <https://doi.org/10.5194/acp-15-3045-2015>, 2015.

733 Liu, Z., Wang, Y., Gu, D., Zhao, C., Huey, L. G., Stickel, R., Liao, J., Shao, M., Zhu, T., Zeng, L.,
734 Amoroso, A., Costabile, F., Chang, C.-C., and Liu, S.-C.: Summertime photochemistry during
735 CAREBeijing-2007: RO_x budgets and O₃ formation, *Atmos. Chem. Phys.*, 12, 7737–7752,
736 <https://doi.org/10.5194/acp-12-7737-2012>, 2012.

737 Liu, Z., Wang, Y., Hu, B., Lu, K., Tang, G., Ji, D., Yang, X., Gao, W., Xie, Y., Liu, J., Yao, D., Yang,
738 Y., and Zhang, Y.: Elucidating the quantitative characterization of atmospheric oxidation capacity

739 in Beijing, China, *Sci. Total Environ.*, 771, 145306,
740 <https://doi.org/10.1016/j.scitotenv.2021.145306>, 2021.

741 Lou, S., Holland, F., Rohrer, F., Lu, K., Bohn, B., Brauers, T., Chang, C. C., Fuchs, H., Haeseler, R.,
742 Kita, K., Kondo, Y., Li, X., Shao, M., Zeng, L., Wahner, A., Zhang, Y., Wang, W., and
743 Hofzumahaus, A.: Atmospheric OH reactivities in the Pearl River Delta - China in summer 2006:
744 measurement and model results, *Atmos. Chem. Phys.*, 10, 11243–11260,
745 <https://doi.org/10.5194/acp-10-11243-2010>, 2010.

746 Luecken, D. J., Hutzell, W. T., Strum, M. L., and Pouliot, G. A.: Regional sources of atmospheric
747 formaldehyde and acetaldehyde, and implications for atmospheric modeling, *Atmos. Environ.*,
748 47, 477–490, <https://doi.org/10.1016/j.atmosenv.2011.10.005>, 2012.

749 McDonald, B. C., de Gouw, J. A., Gilman, J. B., Jathar, S. H., Akherati, A., Cappa, C. D., Jimenez,
750 J. L., Lee-Taylor, J., Hayes, P. L., McKeen, S. A., Cui, Y. Y., Kim, S.-W., Gentner, D. R.,
751 Isaacman-VanWertz, G., Goldstein, A. H., Harley, R. A., Frost, G. J., Roberts, J. M., Ryerson, T.
752 B., and Trainer, M.: Volatile chemical products emerging as largest petrochemical source of urban
753 organic emissions, *Science*, 359, 760–764, <https://doi.org/10.1126/science.aag0524>, 2018.

754 Mo, Z., Shao, M., and Lu, S.: Compilation of a source profile database for hydrocarbon and OVOC
755 emissions in China, *Atmos. Environ.*, 143, 209–217,
756 <https://doi.org/10.1016/j.atmosenv.2016.08.025>, 2016.

757 Mo, Z., Shao, M., Wang, W., Liu, Y., Wang, M., and Lu, S.: Evaluation of biogenic isoprene
758 emissions and their contribution to ozone formation by ground-based measurements in Beijing,
759 China, *Sci. Total Environ.*, 627, 1485–1494, <https://doi.org/10.1016/j.scitotenv.2018.01.336>,
760 2018.

761 Mo, Z., Huang, S., Yuan, B., Pei, C., Song, Q., Qi, J., Wang, M., Wang, B., Wang, C., and Shao, M.:
762 Tower-based measurements of NMHCs and OVOCs in the Pearl River Delta: Vertical distribution,
763 source analysis and chemical reactivity, *Environ. Pollut.*, 292, 118454,
764 <https://doi.org/10.1016/j.envpol.2021.118454>, 2022.

765 Ou, J., Zheng, J., Li, R., Huang, X., Zhong, Z., Zhong, L., and Lin, H.: Speciated OVOC and VOC
766 emission inventories and their implications for reactivity-based ozone control strategy in the Pearl
767 River Delta region, China, *Sci. Total Environ.*, 530, 393–402,
768 <https://doi.org/10.1016/j.scitotenv.2015.05.062>, 2015.

769 Peng, Y., Cai, J., Feng, Y., Jiang, H., and Chen, Y.: Emission characteristic of OVOCs, I/SVOCs,
770 OC and EC from wood combustion at different moisture contents, *Atmos. Environ.*, 298, 119620,
771 <https://doi.org/10.1016/j.atmosenv.2023.119620>, 2023.

772 Pfannerstill, E. Y., Arata, C., Zhu, Q., Schulze, B. C., Woods, R., Harkins, C., Schwantes, R. H.,
773 McDonald, B. C., Seinfeld, J. H., Bucholtz, A., Cohen, R. C., and Goldstein, A. H.: Comparison
774 between Spatially Resolved Airborne Flux Measurements and Emission Inventories of Volatile
775 Organic Compounds in Los Angeles, *Environ. Sci. Technol.*, 57, 15533–15545,
776 <https://doi.org/10.1021/acs.est.3c03162>, 2023.

777 Qin, Z., Xu, B., Zheng, Z., Li, L., Zhang, G., Li, S., Geng, C., Bai, Z., and Yang, W.: Integrating
778 ambient carbonyl compounds provides insight into the constrained ozone formation chemistry in
779 Zibo city of the North China Plain, *Environ. Pollut.*, 324, 121294,
780 <https://doi.org/10.1016/j.envpol.2023.121294>, 2023.

781 Qu, H., Wang, Y., Zhang, R., Liu, X., Huey, L. G., Sjostedt, S., Zeng, L., Lu, K., Wu, Y., Shao, M.,
782 Hu, M., Tan, Z., Fuchs, H., Broch, S., Wahner, A., Zhu, T., and Zhang, Y.: Chemical Production

783 of Oxygenated Volatile Organic Compounds Strongly Enhances Boundary-Layer Oxidation
784 Chemistry and Ozone Production, *Environ. Sci. Technol.*, 55, 13718–13727,
785 <https://doi.org/10.1021/acs.est.1c04489>, 2021.

786 Ren, Q.: Circular economy action programs and countermeasures for small and medium-sized
787 resource-based cities of China-case study of Zibo City of Shandong Province, *Energy Procedia*,
788 2183–2188, <https://doi.org/10.1016/j.egypro.2011.03.377>, 2011.

789 Rieksta, J., Li, T., Davie-Martin, C. L., Aeppli, L. C. B., Hoye, T. T., and Rinnan, R.: Volatile
790 responses of dwarf birch to mimicked insect herbivory and experimental warming at two
791 elevations in Greenlandic tundra., *Plant Environ Interact*, 4, 23–35,
792 <https://doi.org/10.1002/pei3.10100>, 2023.

793 Sarwar, G., Luecken, D., Yarwood, G., Whitten, G. Z., and Carter, W. P. L.: Impact of an updated
794 carbon bond mechanism on predictions from the CMAQ modeling system: Preliminary
795 assessment, *J. Appl. Meteorol. Climatol.*, 47, 3–14, <https://doi.org/10.1175/2007JAMC1393.1>,
796 2008.

797 Saunders, S. M., Jenkin, M. E., Derwent, R. G., and Pilling, M. J.: Protocol for the development of
798 the Master Chemical Mechanism, MCM v3 (Part A): tropospheric degradation of non-aromatic
799 volatile organic compounds, *Atmos. Chem. Phys.*, 3, 161–180, [https://doi.org/10.5194/acp-3-](https://doi.org/10.5194/acp-3-161-2003)
800 161-2003, 2003.

801 Shen, L., Jacob, D. J., Zhu, L., Zhang, Q., Zheng, B., Sulprizio, M. P., Li, K., De Smedt, I., Abad,
802 G. G., Cao, H., Fu, T.-M., and Liao, H.: The 2005-2016 Trends of Formaldehyde Columns Over
803 China Observed by Satellites: Increasing Anthropogenic Emissions of Volatile Organic
804 Compounds and Decreasing Agricultural Fire Emissions, *Geophys. Res. Lett.*, 46, 4468–4475,
805 <https://doi.org/10.1029/2019GL082172>, 2019.

806 Sindelarova, K., Granier, C., Bouarar, I., Guenther, A., Tilmes, S., Stavrou, T., Muller, J.-F., Kuhn,
807 U., Stefani, P., and Knorr, W.: Global data set of biogenic VOC emissions calculated by the
808 MEGAN model over the last 30 years, *Atmos. Chem. Phys.*, 14, 9317–9341,
809 <https://doi.org/10.5194/acp-14-9317-2014>, 2014.

810 Song, J., Saathoff, H., Jiang, F., Gao, L., Zhang, H., and Leisner, T.: Sources of organic gases and
811 aerosol particles and their roles in nighttime particle growth at a rural forested site in southwest
812 Germany, *Atmos. Chem. Phys.*, 24, 6699–6717, <https://doi.org/10.5194/acp-24-6699-2024>, 2024.

813 Song, M., Li, X., Yang, S., Yu, X., Zhou, S., Yang, Y., Chen, S., Dong, H., Liao, K., Chen, Q., Lu,
814 K., Zhang, N., Cao, J., Zeng, L., and Zhang, Y.: Spatiotemporal variation, sources, and secondary
815 transformation potential of volatile organic compounds in Xi'an, China, *Atmos. Chem. Phys.*, 21,
816 4939–4958, <https://doi.org/10.5194/acp-21-4939-2021>, 2021.

817 Steiner, A. L., Cohen, R. C., Harley, R. A., Tonse, S., Millet, D. B., Schade, G. W., and Goldstein,
818 A. H.: VOC reactivity in central California: comparing an air quality model to ground-based
819 measurements, *Atmos. Chem. Phys.*, 8, 351–368, <https://doi.org/10.5194/acp-8-351-2008>, 2008.

820 Stockwell, W. R., Kirchner, F., Kuhn, M., and Seefeld, S.: A new mechanism for regional
821 atmospheric chemistry modeling, *J. Geophys. Res.-Atmos.*, 102, 25847–25879,
822 <https://doi.org/10.1029/97JD00849>, 1997a.

823 Stockwell, W. R., Kirchner, F., Kuhn, M., and Seefeld, S.: A new mechanism for regional
824 atmospheric chemistry modeling, *J. Geophys. Res.-Atmos.*, 102, 25847–25879,
825 <https://doi.org/10.1029/97JD00849>, 1997b.

826 Tan, Z., Fuchs, H., Lu, K., Hofzumahaus, A., Bohn, B., Broch, S., Dong, H., Gomm, S., Haeseler,

827 R., He, L., Holland, F., Li, X., Liu, Y., Lu, S., Rohrer, F., Shao, M., Wang, B., Wang, M., Wu, Y.,
828 Zeng, L., Zhang, Y., Wahner, A., and Zhang, Y.: Radical chemistry at a rural site (Wangdu) in the
829 North China Plain: observation and model calculations of OH, HO₂ and RO₂ radicals, *Atmos.*
830 *Chem. Phys.*, 17, 663–690, <https://doi.org/10.5194/acp-17-663-2017>, 2017.

831 Tan, Z., Lu, K., Jiang, M., Su, R., Dong, H., Zeng, L., Xie, S., Tan, Q., and Zhang, Y.: Exploring
832 ozone pollution in Chengdu, southwestern China: A case study from radical chemistry to O₃-
833 VOC-NO_x sensitivity, *Sci. Total Environ.*, 636, 775–786,
834 <https://doi.org/10.1016/j.scitotenv.2018.04.286>, 2018a.

835 Tan, Z., Rohrer, F., Lu, K., Ma, X., Bohn, B., Broch, S., Dong, H., Fuchs, H., Gkatzelis, G. I.,
836 Hofzumahaus, A., Holland, F., Li, X., Liu, Y., Liu, Y., Novelli, A., Shao, M., Wang, H., Wu, Y.,
837 Zeng, L., Hu, M., Kiendler-Scharr, A., Wahner, A., and Zhang, Y.: Wintertime photochemistry in
838 Beijing: observations of RO_x radical concentrations in the North China Plain during the BEST-
839 ONE campaign, *Atmos. Chem. Phys.*, 18, 12391–12411, [https://doi.org/10.5194/acp-18-12391-](https://doi.org/10.5194/acp-18-12391-2018)
840 2018, 2018b.

841 Tan, Z., Lu, K., Jiang, M., Su, R., Wang, H., Lou, S., Fu, Q., Zhai, C., Tan, Q., Yue, D., Chen, D.,
842 Wang, Z., Xie, S., Zeng, L., and Zhang, Y.: Daytime atmospheric oxidation capacity in four
843 Chinese megacities during the photochemically polluted season: a case study based on box model
844 simulation, *Atmos. Chem. Phys.*, 19, 3493–3513, <https://doi.org/10.5194/acp-19-3493-2019>,
845 2019a.

846 Tan, Z., Lu, K., Hofzumahaus, A., Fuchs, H., Bohn, B., Holland, F., Liu, Y., Rohrer, F., Shao, M.,
847 Sun, K., Wu, Y., Zeng, L., Zhang, Y., Zou, Q., Kiendler-Scharr, A., Wahner, A., and Zhang, Y.:
848 Experimental budgets of OH, HO₂, and RO₂ radicals and implications for ozone formation in the
849 Pearl River Delta in China 2014, *Atmos. Chem. Phys.*, 19, 7129–7150,
850 <https://doi.org/10.5194/acp-19-7129-2019>, 2019b.

851 Venecek, M. A., Carter, W. P. L., and Kleeman, M. J.: Updating the SAPRC Maximum Incremental
852 Reactivity (MIR) scale for the United States from 1988 to 2010, *J. Air Waste Manage. Assoc.*, 68,
853 1301–1316, <https://doi.org/10.1080/10962247.2018.1498410>, 2018.

854 Volkamer, R., Sheehy, P., Molina, L. T., and Molina, M. J.: Oxidative capacity of the Mexico City
855 atmosphere - Part 1: A radical source perspective, *Atmos. Chem. Phys.*, 10, 6969–6991,
856 <https://doi.org/10.5194/acp-10-6969-2010>, 2010.

857 Wang, G., Zhu, Z., Liu, Z., Liu, X., Kong, F., Nie, L., Gao, W., Zhao, N., and Lang, J.: Ozone
858 pollution in the plate and logistics capital of China: Insight into the formation, source
859 apportionment, and regional transport, *Environ. Pollut.*, 313,
860 <https://doi.org/10.1016/j.envpol.2022.120144>, 2022a.

861 Wang, M., Zeng, L., Lu, S., Shao, M., Liu, X., Yu, X., Chen, W., Yuan, B., Zhang, Q., Hu, M., and
862 Zhang, Z.: Development and validation of a cryogen-free automatic gas chromatograph system
863 (GC-MS/FID) for online measurements of volatile organic compounds, *Anal. Methods*, 6, 9424–
864 9434, <https://doi.org/10.1039/C4AY01855A>, 2014.

865 Wang, R., Wang, L., Yang, Y., Zhan, J., Ji, D., Hu, B., Ling, Z., Xue, M., Zhao, S., Yao, D., Liu, Y.,
866 and Wang, Y.: Comparative analysis for the impacts of VOC subgroups and atmospheric
867 oxidation capacity on O₃ based on different observation-based methods at a suburban site in the
868 North China Plain, *Environ. Res.*, 248, 118250, <https://doi.org/10.1016/j.envres.2024.118250>,
869 2024.

870 Wang, S., Yuan, B., Wu, C., Wang, C., Li, T., He, X., Huangfu, Y., Qi, J., Li, X.-B., Sha, Q., Zhu,

871 M., Lou, S., Wang, H., Karl, T., Graus, M., Yuan, Z., and Shao, M.: Oxygenated volatile organic
872 compounds (VOCs) as significant but varied contributors to VOC emissions from vehicles,
873 *Atmos. Chem. Phys.*, 22, 9703–9720, <https://doi.org/10.5194/acp-22-9703-2022>, 2022b.

874 Wang, S., Zhang, J., Zhang, Y., Wang, L., Sun, Z., and Wang, H.: Review on Source Profiles of
875 Volatile Organic Compounds (VOCs) in Typical Industries in China, *Atmosphere*, 14, 878,
876 <https://doi.org/10.3390/atmos14050878>, 2023.

877 Wang, W., Yuan, B., Peng, Y., Su, H., Cheng, Y., Yang, S., Wu, C., Qi, J., Bao, F., Huangfu, Y., Wang,
878 C., Ye, C., Wang, Z., Wang, B., Wang, X., Song, W., Hu, W., Cheng, P., Zhu, M., Zheng, J., and
879 Shao, M.: Direct observations indicate photodegradable oxygenated volatile organic compounds
880 (OVOCs) as larger contributors to radicals and ozone production in the atmosphere, *Atmos. Chem.*
881 *Phys.*, 22, 4117–4128, <https://doi.org/10.5194/acp-22-4117-2022>, 2022c.

882 Wolfe, G. M., Marvin, M. R., Roberts, S. J., Travis, K. R., and Liao, J.: The Framework for 0-D
883 Atmospheric Modeling (F0AM) v3.1, *Geosci. Model Dev.*, 9, 3309–3319,
884 <https://doi.org/10.5194/gmd-9-3309-2016>, 2016.

885 Wu, Y., Fan, X., Liu, Y., Zhang, J., Wang, H., Sun, L., Fang, T., Mao, H., Hu, J., Wu, L., Peng, J.,
886 and Wang, S.: Source apportionment of VOCs based on photochemical loss in summer at a
887 suburban site in Beijing, *Atmos. Environ.*, 293, 119459,
888 <https://doi.org/10.1016/j.atmosenv.2022.119459>, 2023.

889 Xia, S.-Y., Wang, C., Zhu, B., Chen, X., Feng, N., Yu, G.-H., and Huang, X.-F.: Long-term
890 observations of oxygenated volatile organic compounds (OVOCs) in an urban atmosphere in
891 southern China, 2014–2019, *Environ. Pollut.*, 270, 116301,
892 <https://doi.org/10.1016/j.envpol.2020.116301>, 2021.

893 Xu, Z., Wang, T., Xue, L. K., Louie, P. K. K., Luk, C. W. Y., Gao, J., Wang, S. L., Chai, F. H., and
894 Wang, W. X.: Evaluating the uncertainties of thermal catalytic conversion in measuring
895 atmospheric nitrogen dioxide at four differently polluted sites in China, *Atmos. Environ.*, 76,
896 221–226, <https://doi.org/10.1016/j.atmosenv.2012.09.043>, 2013.

897 Xuan, H., Zhao, Y., Ma, Q., Chen, T., Liu, J., Wang, Y., Liu, C., Wang, Y., Liu, Y., Mu, Y., and He,
898 H.: Formation mechanisms and atmospheric implications of summertime nitrous acid (HONO)
899 during clean, ozone pollution and double high-level PM_{2.5} and O₃ pollution periods in Beijing,
900 *Sci. Total Environ.*, 857, 159538, <https://doi.org/10.1016/j.scitotenv.2022.159538>, 2023.

901 Xue, L., Wang, T., Louie, P. K. K., Luk, C. W. Y., Blake, D. R., and Xu, Z.: Increasing External
902 Effects Negate Local Efforts to Control Ozone Air Pollution: A Case Study of Hong Kong and
903 Implications for Other Chinese Cities, *Environ. Sci. Technol.*, 48, 10769–10775,
904 <https://doi.org/10.1021/es503278g>, 2014a.

905 Xue, L., Gu, R., Wang, T., Wang, X., Saunders, S., Blake, D., Louie, P. K. K., Luk, C. W. Y., Simpson,
906 I., Xu, Z., Wang, Z., Gao, Y., Lee, S., Mellouki, A., and Wang, W.: Oxidative capacity and radical
907 chemistry in the polluted atmosphere of HongKong and Pearl River Delta region: analysis of a
908 severe photochemical smog episode, *Atmos. Chem. Phys.*, 16, 9891–9903,
909 <https://doi.org/10.5194/acp-16-9891-2016>, 2016.

910 Xue, L. K., Wang, T., Gao, J., Ding, A. J., Zhou, X. H., Blake, D. R., Wang, X. F., Saunders, S. M.,
911 Fan, S. J., Zuo, H. C., Zhang, Q. Z., and Wang, W. X.: Ground-level ozone in four Chinese cities:
912 precursors, regional transport and heterogeneous processes, *Atmos. Chem. Phys.*, 14, 13175–
913 13188, <https://doi.org/10.5194/acp-14-13175-2014>, 2014b.

914 Yang, C., Yao, N., Xu, L., Chen, G., Wang, Y., Fan, X., Zhou, P., Clusius, P., Tham, Y. J., Lin, Z.,

915 Chen, Y., Li, M., Hong, Y., and Chen, J.: Molecular Composition of Anthropogenic Oxygenated
916 Organic Molecules and Their Contribution to Organic Aerosol in a Coastal City, *Environ. Sci.*
917 *Technol.*, 57, 15956–15967, <https://doi.org/10.1021/acs.est.3c03244>, 2023.

918 Yang, M., Beale, R., Liss, P., Johnson, M., Blomquist, B., and Nightingale, P.: Air-sea fluxes of
919 oxygenated volatile organic compounds across the Atlantic Ocean, *Atmos. Chem. Phys.*, 14,
920 7499–7517, <https://doi.org/10.5194/acp-14-7499-2014>, 2014.

921 Yang, X., Xue, L., Wang, T., Wang, X., Gao, J., Lee, S., Blake, D. R., Chai, F., and Wang, W.:
922 Observations and Explicit Modeling of Summertime Carbonyl Formation in Beijing:
923 Identification of Key Precursor Species and Their Impact on Atmospheric Oxidation Chemistry,
924 *J. Geophys. Res.-Atmos.*, 123, 1426–1440, <https://doi.org/10.1002/2017JD027403>, 2018.

925 Yang, X., Cheng, X., Yan, H., Sun, Y., and Zhang, G.: Ground-Level Ozone Production over an
926 Industrial Cluster of China: a Box Model Analysis of a Severe Photochemical Pollution Episode,
927 *Pol. J. Environ. Stud.*, 31, 1885–1899, <https://doi.org/10.15244/pjoes/143253>, 2022a.

928 Yang, X., Lu, K., Ma, X., Gao, Y., Tan, Z., Wang, H., Chen, X., Li, X., Huang, X., He, L., Tang, M.,
929 Zhu, B., Chen, S., Dong, H., Zeng, L., and Zhang, Y.: Radical chemistry in the Pearl River Delta:
930 observations and modeling of OH and HO₂ radicals in Shenzhen in 2018, *Atmos. Chem. Phys.*,
931 22, 12525–12542, <https://doi.org/10.5194/acp-22-12525-2022>, 2022b.

932 Yarwood, G., Rao, S., Way, R., Yocke, M., Whitten, G. Z., and Reyes, S.: Deborah Luecken U.S.
933 Environmental Protection Agency Research Triangle Park, NC 27703, 2005.

934 Yarwood, G., Jung, J., Whitten, G. Z., Heo, G., Mellberg, J., and Estes, M.: Updates to the Carbon
935 Bond mechanism for version 6 (CB6), 2010.

936 Yokelson, R. J., Karl, T., Artaxo, P., Blake, D. R., Christian, T. J., Griffith, D. W. T., Guenther, A.,
937 and Hao, W. M.: The Tropical Forest and Fire Emissions Experiment: overview and airborne fire
938 emission factor measurements, *Atmos. Chem. Phys.*, 7, 5175–5196, <https://doi.org/10.5194/acp-7-5175-2007>, 2007.

940 Zhang, K., Huang, L., Li, Q., Huo, J., Duan, Y., Wang, Y., Yaluk, E., Wang, Y., Fu, Q., and Li, L.:
941 Explicit modeling of isoprene chemical processing in polluted air masses in suburban areas of the
942 Yangtze River Delta region: radical cycling and formation of ozone and formaldehyde, *Atmos.*
943 *Chem. Phys.*, 21, 5905–5917, <https://doi.org/10.5194/acp-21-5905-2021>, 2021a.

944 Zhang, K., Duan, Y., Huo, J., Huang, L., Wang, Y., Fu, Q., Wang, Y., and Li, L.: Formation
945 mechanism of HCHO pollution in the suburban Yangtze River Delta region, China: A box model
946 study and policy implementations, *Atmos. Environ.*, 267, 118755,
947 <https://doi.org/10.1016/j.atmosenv.2021.118755>, 2021b.

948 Zhang, Z., Sun, Y., and Li, J.: Characteristics and sources of VOCs in a coastal city in eastern China
949 and the implications in secondary organic aerosol and O₃ formation, *Sci. Total Environ.*, 887,
950 164117, <https://doi.org/10.1016/j.scitotenv.2023.164117>, 2023.

951 Zheng, B., Zhang, Q., Geng, G., Chen, C., Shi, Q., Cui, M., Lei, Y., and He, K.: Changes in China's
952 anthropogenic emissions and air quality during the COVID-19 pandemic in 2020, *Earth Syst. Sci.*
953 *Data*, 13, 2895–2907, <https://doi.org/10.5194/essd-13-2895-2021>, 2021.

954 Zheng, Z., Li, K., Xu, B., Dou, J., Li, L., Zhang, G., Li, S., Geng, C., Yang, W., Azzi, M., and Bai,
955 Z.: O₃-precursor relationship over multiple patterns of timescale: a case study in Zibo, Shandong
956 Province, China, *Atmos. Chem. Phys.*, 23, 2649–2665, <https://doi.org/10.5194/acp-23-2649-2023>,
957 2023.

958 Zhou, J., Zhang, C., Liu, A., Yuan, B., Wang, Y., Wang, W., Zhou, J.-P., Hao, Y., Li, X.-B., He, X.,

959 Song, X., Chen, Y., Yang, S., Yang, S., Wu, Y., Jiang, B., Huang, S., Liu, J., Peng, Y., Qi, J., Deng,
960 M., Zhong, B., Huangfu, Y., and Shao, M.: Measurement report: Vertical and temporal variability
961 in the near-surface ozone production rate and sensitivity in an urban area in the Pearl River Delta
962 region, China, *Atmos. Chem. Phys.*, 24, 9805–9826, <https://doi.org/10.5194/acp-24-9805-2024>,
963 2024.

964 Zhou, M., Jiang, W., Gao, W., Gao, X., Ma, M., and Ma, X.: Anthropogenic emission inventory of
965 multiple air pollutants and their spatiotemporal variations in 2017 for the Shandong Province,
966 China*, *Environ. Pollut.*, 288, 117666, <https://doi.org/10.1016/j.envpol.2021.117666>, 2021.

967 Zhu, J., Wang, S., Wang, H., Jing, S., Lou, S., Saiz-Lopez, A., and Zhou, B.: Observationally
968 constrained modeling of atmospheric oxidation capacity and photochemical reactivity in
969 Shanghai, China, *Atmos. Chem. Phys.*, 20, 1217–1232, [https://doi.org/10.5194/acp-20-1217-](https://doi.org/10.5194/acp-20-1217-2020)
970 2020, 2020.

971